food colorants, cosmetics, and toothpastes. To evaluate its toxicity, reference substances are required to characterize dose, dimension, and durability (Donaldson et al. 2004; Maynard 2006; Nel et al. 2006; Oberdorster et al. 2005; Soto et al. 2005; Warheit et al. 2008; Yang et al. 2009). As a detection method of nanoparticles, inductively coupled plasma mass spectrometer (ICP-MS) was used to calculate the amount of nanomaterials in organs (De Jong et al. 2008; Fabian et al. 2008; Wang et al. 2007), however, it could not show the localized nanoparticles in the cellular level. Cellular distribution and the effects of nanoparticles analyzed by field emission-scanning electron microscope/energy dispersive X-ray spectroscopy (FE-SEM/EDS) is an issue (Chen et al. 2011; Komatsu et al. 2008; Patri et al. 2009; Umbreit et al. 2011). Transmission electron microscopic (TEM) sections through cells, tissues, and organs for quantifying nanoparticles were reviewed to be efficient (Mayhew et al. 2009).

The effect of nanoparticle exposure and testicular dysfunction have been reported that inhalation to diesel exhaust particles ($\sim 1 \times 10^6$ particles/cm^3, 240 nm with the mass median diameter in the air) during pregnancy reduced daily sperm production (DSP) in adulthood without altering endocrine function or expression in the testes (Hemmingsen et al. 2009), and that maternal airway exposure to nano-TiO_2 (1.7×10^6 particles/cm^3 aerosolized powder, 97 nm of major particle size) was tended to reduce sperm count (Kyjovska et al. 2013) .

In a previous study, we examined the effect of a 400 μg dose exposure of anatase-type nano-TiO_2 (25–70 nm) on pregnant mice by dorsal subcutaneous injection was shown to cause testicular dysfunction in male offspring. The shift of nano-TiO_2 from the mother's body to offspring testis was confirmed by FE-SEM/EDS which showed that these nanoparticles contain Ti by the characteristic peak on 4.51 keV (Takeda et al. 2009). In addition to our previous study, the effects of prenatal exposure to carbon black 200 μg (14 nm) doses administered to pregnant mice were shown to affect reproductive function through damage to the seminiferous epithelium and reduction of DSP in male offspring (Yoshida et al. 2010). These studies have examined the higher doses nanoparticles administered to pregnant mice. Nanomaterials were demonstrated to easily cross the placental barrier with the diameter up to 240 nm in an ex vivo human placental perfusion (Wick et al. 2010) and with that of 70 nm in the 800 μg dose intravenous injection per pregnant mice (Yamashita et al. 2011). It is not currently investigated whether low-dose nanoparticles exposure during pregnancy would effect on the offspring testis.

In this study, we evaluated the dose–dependent biodistribution of prenatal exposure to rutile-type nano-TiO_2 on mice testes in 12-week-old offspring by SEM and TEM.

Materials and methods

Animals

Pregnant ICR mice (2 days postcoitum) were purchased from SLC Co. (Shizuoka, Japan) and divided into four nano-TiO_2 recipient groups and a control group. They were maintained in a temperature- and light-controlled environment (12-h light/12-h dark cycle) with ad libitum access to standard rodent food and water. The treatment and care of all mice were approved by the Animal Care and Use Committee of the Tokyo University of Science.

Characterization of rutile nano-TiO_2

Rutile-type nano-TiO_2 powder of 35 nm with primary diameter was provided by Tayca Co. (Osaka, Japan). The powder was suspended at 1 mg/ml in saline (Otsuka Pharmaceutical Factory Inc., Tokushima, Japan) containing 0.05 % Tween 80 and sonicated for 30 min immediately before subcutaneous injection. Tenfold serial dilutions (1, 10, 100, and 1,000 μg/ml) obtained from the middle layer of the original suspension were prepared to examine the size distribution of nano-TiO_2. Dynamic light scattering (DLS) measurement with Nano-ZS (Sysmex Co., Kobe, Hyogo, Japan) was applied three times for each dose suspension. To observe the dispersed nano-TiO_2 in suspensions, a drop of the suspension was placed on formvar-coated copper grids, which were fully drained off and allowed to air dry. A SEM (JEM-6500F JEOL, Tokyo) with elemental analysis by EDS was used at the same time to identify the presence of Ti element in the seminiferous epithelium. The size and shape of visualized nanoparticles were observed by a JEM 1200EX II TEM (JEOL Ltd., Tokyo, Japan).

Injection of nano-TiO_2

Pregnant mice divided into four nano-TiO_2 recipient groups and control group were injected subcutaneously according to the method described by Sharpe et al. (1998). In the recipient groups, each mouse was injected with 0.1 ml of 1, 10, 100, or 1,000 μg/ml of rutile-type nano-TiO_2 suspension studied in the last section, once each on gestational days 5, 8, 11, 14, and 17. The mice of each group received total doses of 0.5, 5, 50, and 500 μg, respectively. The mice of the control group received 0.1 ml of saline with 0.05 % Tween 80 injected in the same manner. The offspring testes were examined at 12 weeks postpartum.

Semi-quantitative evaluation of the nanoparticles in the seminiferous epithelium by electron microscopy

Three animals were selected (one per litter) for the examination. The dissected testes were directly fixed with 2.5 % glutaraldehyde in 0.2 M sodium cacodylate buffer overnight at 4 °C. After washing in the same buffer, samples were post-fixed in 2 % OsO_4 for 1 h, dehydrated in graded series of ethanol, and embedded in epoxy resin. Ultra-thin (100-nm thickness) sections cut on a Sorvall ultra-microtome MT-2 (Leica Mikrosystem LTD GmbH, Vienna, Austria) for detection of agglomerates in the seminiferous epithelium. Based on SEM and TEM observations of the ultrathin sections adapted from Mayhew et al. (2009), the agglomerates found in a unit (1-μm^2 area) of sections on a grid (200 meshes NISSHIN EM Co. Ltd., Japan) and the number of units on five grids was totalled. The number of agglomerates was then roughly estimated for the 0.5, 5, 50, and 500 μg recipient groups. For ultrastructural observations of the seminiferous epithelium, ultrathin (80 nm thick) sections stained doubly with uranyl acetate and lead citrate.

Results

The nano-TiO_2 injections to pregnant mice

The scheme of rutile-type nano-TiO_2 injections is shown in Fig. 1a. Pregnant mice injected five times with 0.1 ml suspensions received total doses of 0.5, 5, 50, and 500 μg, respectively. The mice delivered their pups on gestational day 19. In the 0, 0.5, 5, 50, and 500 μg recipient groups, the numbers of dams and male to female sex ratios of pups for each group were, respectively, as follows: 4 (dams) and 46 (25 males:21 females); 4 and 52 (26:26); 4 and 56 (27:28); 6 and 69 (40:29); and 5 and 52 (24:28). Pups in each group were weaned on postnatal 21. Male reproductive organs developed fully and no structural malformations were observed. There were no differences observed in general toxicity between the control and the nano-TiO_2-recipient groups during the 12 weeks postpartum.

Characterization of rutile-type nano-TiO_2

The characterization of rutile-type nano-TiO_2 provided by Tayca Co. is shown in Table 1. The most diluted concentration, 1 μg/ml suspensions in saline containing 0.05 % Tween 80, demonstrated that agglomerates with various sizes except few large particles were dispersed well under SEM (Fig. 1b). Under TEM (Fig. 1c) measurement, individual agglomerate below the size around 200 nm were recognized to be spherical or rod shape as a whole and constructed with many nano-TiO_2 particles of 35 nm with primary diameter and held together. The suspensions analyzed using DLS measurement included the intensity-weighted average diameter over all size population (Zeta-average) and the polydispersity index (PDI). The average diameter was increased in a dose–dependent manner; 1–1,000 μg/ml suspensions were from 193.3 ± 5.4 to 1980.3 ± 95.8 nm in diameter (Table and Graph inset in Fig. 1d). Standard deviations of each dose suspension were indicated in the graph. The DLS measurement of the 1 μg/ml suspensions was similar to small agglomerates below 200 nm recognized under SEM (Fig. 1b) and TEM (Fig. 1c).

Detection of rutile-type nano-TiO_2 in the testicular sections of offspring at 12 weeks

At high magnification under TEM, some unambiguous electron dense particles were found in the Sertoli cell cytoplasm of the 0.5 μg recipient group (Fig. 2a). There were loose adhesions around the Sertoli cell with many vacuoles and a deformed sperm nucleus with a part of uncondensed chromatin. To confirm

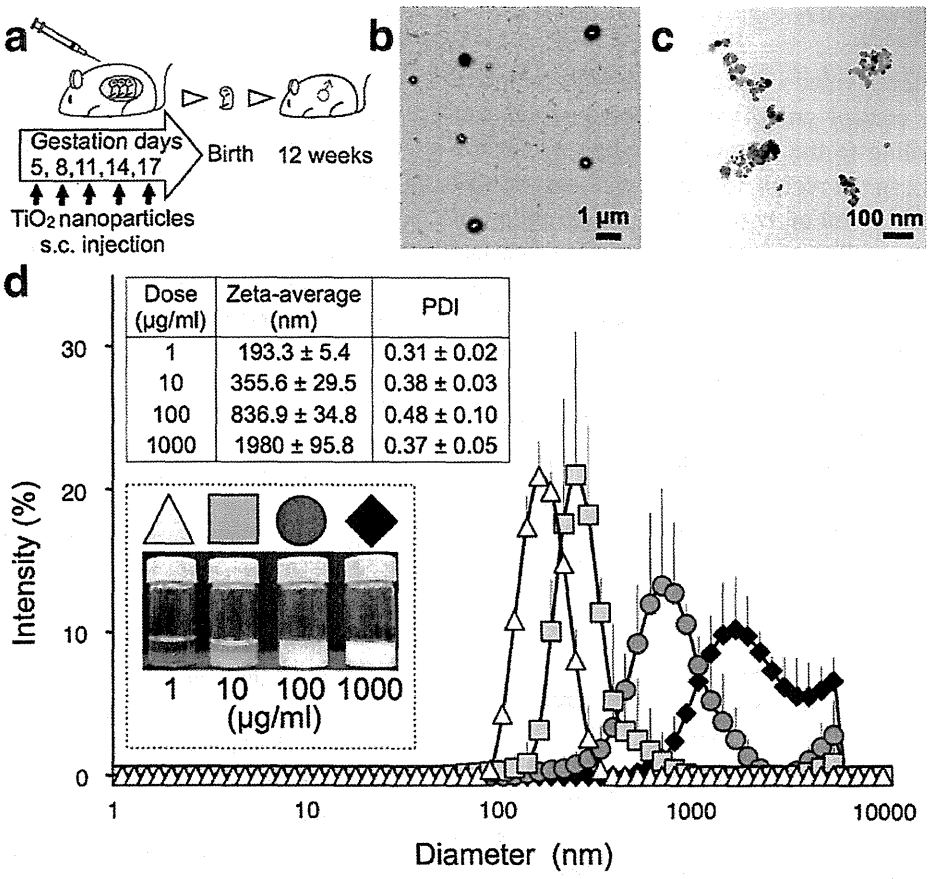

Fig. 1 Scheme of nano-TiO_2 injection and characterization of nano-TiO_2 dosage suspensions. **a** Subcutaneous injection into pregnant ICR mice; 0.1 ml of 1, 10, 100, or 1,000 μg/ml of rutile-type nano-TiO_2 dose on gestational days 5, 8, 11, 14, and 17. The mice of each group received total doses of 0.5, 5, 50, and 500 μg, respectively. **b** SEM images of many small agglomerates below 200 nm dispersed in the most diluted 1 μg/ml suspension. **c** TEM image, with 10 times higher magnification than SEM image, indicates spherical or rod shapes agglomerates below 200 nm are composed of spherical TiO_2 with primary diameter around 35 nm in the same suspension. **d** Characterization of nano-TiO_2 suspensions of tenfold serial dilutions. The diluted solution with 0.05 % Tween 80 to 1, 10, 100, or 1,000 μg/ml analyzed by DLS. The intensity-weighted average diameter over all size population (Zeta-average) and the PDI were shown in Table *inset*. The average diameter was increased in a dose–dependent manner

Table 1 Characterization of rutile-type TiO_2 powder provided by Tayca Co.

Appearance	White powder
TiO^2 (%)	Min 96
pH	Neutral
Cristal structure	Rutile
Property of surface	Hydrophilic
Particle size (nm)	35
Specific surface area	30–50 (m^2/g)

whether the particles contained the Ti element or not, FE-SEM/X-ray spectroscopy were performed to localize nano-TiO_2 (Fig. 2b) and the X-ray spectrum indicated the contain Ti by the characteristic peak on 4.51 keV in the same observed particles (Fig. 2c). The small agglomerate composed of some nano-TiO_2 was found in the Sertoli cell cytoplasm of the 5 μg recipient group. Sertoli cells demonstrated phagocytic functions which suggested that multivesicular vesicles contained damaged mitochondria and small vesicles (Fig. 2d). The small agglomerate was also located in the cytoplasm of the spermatid in the 50 μg recipient group (Fig. 2e) and was positioned beside a developing acrosome enveloped a part of the mid-spermatid nucleus with dispersed chromatin in 500 μg recipient group (Fig. 2f). This indicated that the small agglomerate in the seminiferous epithelium was composed of

nano-TiO_2 35 nm in primary diameter in across all recipient groups. A correlation between nano-TiO_2 doses injected to pregnant mice, and the number of agglomerates in the seminiferous epithelium was demonstrated by the semi-quantitative evaluation (Fig. 2g).

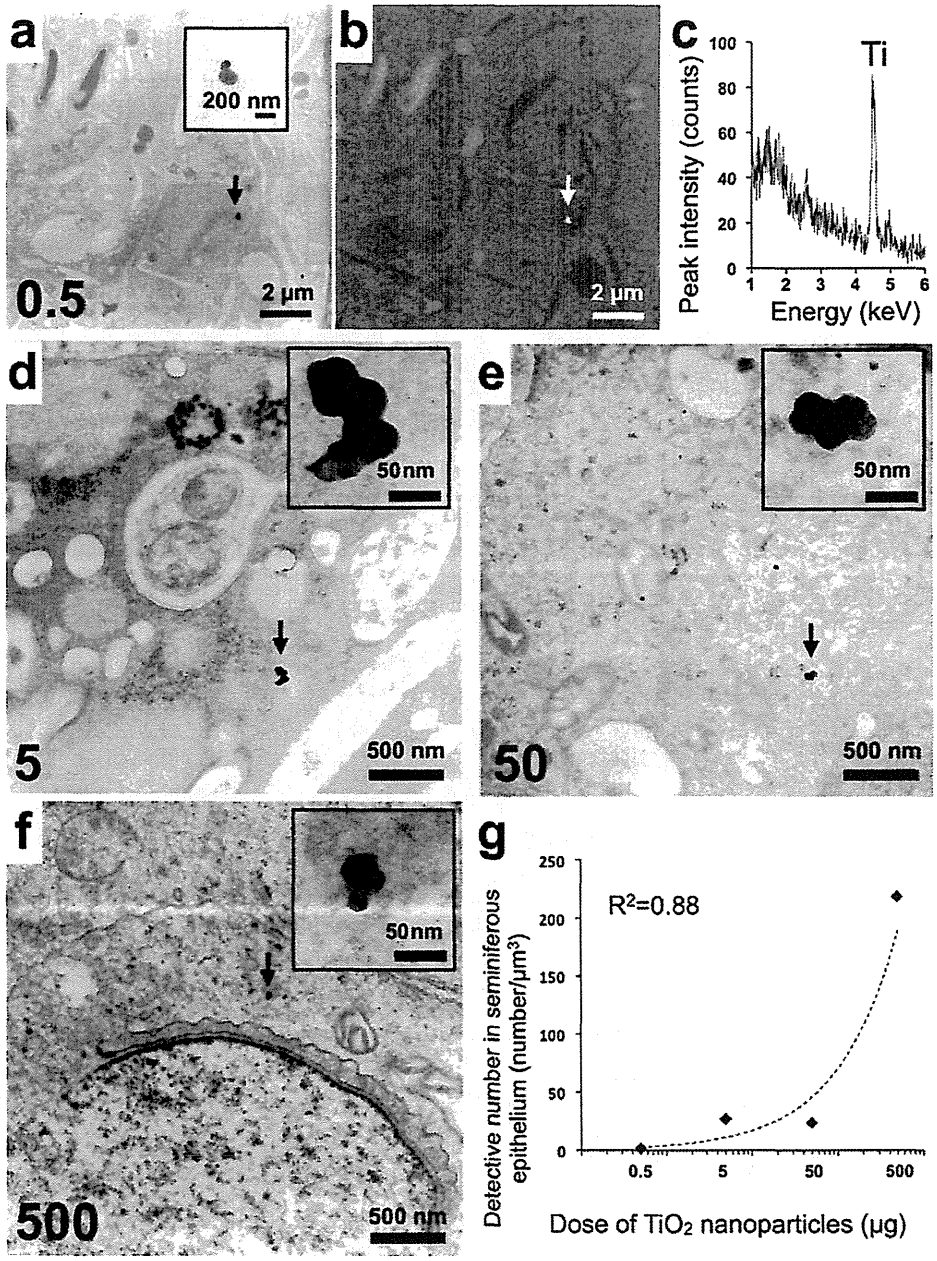

Fig. 2 Nano-TiO_2 in the seminiferous epithelium. **a** TEM image of the seminiferous epithelium in the 0.5 μg group. A *black arrow* shows electron dense particles in the Sertoli cell. The *inset* indicates a small agglomerate of a few nanoparticles. **b** SEM images of the same TEM micrograph. A *white arrow* shows the same agglomerate. **c** X-ray spectrometry indicates Ti peaks on 4.51 keV in the same agglomerate. This observation revealed nano-TiO_2 transferred from pregnant mice to offspring testes. **d** The small agglomerate (*black arrow*) in the cytoplasm of Sertoli cell in the 5 μg group. The *inset* indicates the agglomerate of nano-TiO_2. **e**, **f** The agglomerate (*black arrow*) in the cytoplasm of spermatids in the 50 and 500 μg groups. The *inset* shows the agglomerate of nano-TiO_2. **g** Semi-quantitative evaluation of the nano-TiO_2 in the seminiferous epithelium. The standard curve shows the dose–dependent relationship when nano-TiO_2 are injected at sufficiently high doses

Ultrastructural observations

Electron microscopic observations were performed to examine the seminiferous epithelium in greater detail. In the control group, spermatogenesis advanced normally with spermatogenic cells orientated from the basal to the adluminal compartment and mature spermatozoa were individually released from Sertoli cells into the adluminal lumen (spermiation). Sertoli cells regularly positioned at the basement membrane had a large nucleus with a few nucleoli and the cytoplasm closely contacted the neighboring spermatogenic cells (Fig. 3a). In the 0.5 μg recipient group, a cluster of mature sperm enveloped by the Sertoli cell cytoplasm was positioned at the basal compartment (Fig. 3b). Similar sperm heads at the basal compartment were observed in the other doses recipient groups. Loose adhesion between spermatogenic cells was found in the seminiferous epithelium in the 5 and 50 μg recipient groups (Figs. 3c, d). In the 500 μg recipient group, the sperm head covered irregularly with acrosome was found. The cytoplasm of Sertoli cell around sperm heads showed vacuolization with many electron dense vesicles (Fig. 3e).

In the adluminal lumen, Sertoli cells engulfed a sperm head with an elongated acrosome and two

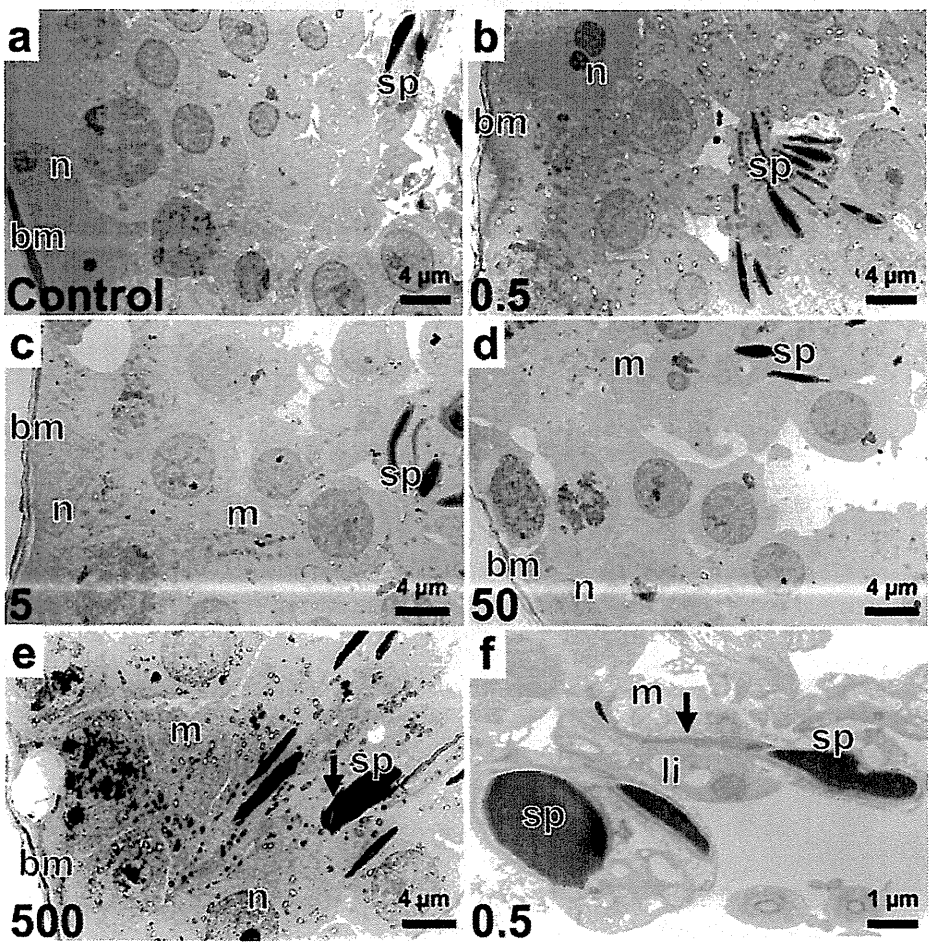

Fig. 3 Ultrastructural alteration of the seminiferous epithelium. **a** Control group: mature spermatozoa released individually into the lumen (spermiation). The Sertoli cell was positioned at the basement membrane and the cytoplasm closely contacted the neighboring spermatogenic cells. **b**, **c** A cluster of mature sperm nuclei located at the basal compartment in the 0.5 and 5 μg groups. **d** The Sertoli cell lost cell adhesion between the neighboring spermatogenic cells in the 50 μg group. **e** A sperm head irregularly covered with acrosome (*black arrow*) was located at the basal compartment. Sertoli cells around sperm heads showed vacuolization in the 500 μg group. **f** An abnormal sperm head with elongated acrosome (*black arrow*) in the 0.5 μg group. The cytoplasm engulfed sperm nuclei had many lipid droplets, Golgi body, and collapsed cristae of mitochondria. *bm* basement membrane, *li* lipid droplets, *m* mitochondria, *n* Sertoli cell nucleus, *sp* mature sperm head

sperm nuclei in the cytoplasm which had lipid droplets, Golgi body, and collapsed cristae of mitochondria in the 0.5 μg recipient group The Sertoli cells indicated the phagocytic activity to eliminate abnormal spermatozoa (Fig. 3f). Similar effects were observed in other nano-TiO_2 recipient groups.

Discussion

The present study has first demonstrated rutile-type nano-TiO_2 in suspensions and in the offspring testis of pregnant mice treated by subcutaneous injection. In the suspension prior to injection, DLS measurement showed that under the most diluted suspension the nano-TiO_2 formed small agglomerates as Nanometer sized, 193.3 ± 5.4 nm in average diameter. In the original suspension, they formed large agglomerates as micron sized 1980.3 ± 95.8 nm in average diameter. At the sequentially diluted of 1–1,000 μg/ml suspensions, the agglomerates sizes decreased with diluting concentrations. They were obviously composed of about 35 nm in primary diameter (Figs. 1c). This phenomenon indicated that the increased concentrations led to increase agglomerates of nano-TiO_2 in the suspensions.

Furthermore, we observed dose–dependent translocation of nano-TiO_2 across the placental barrier and biodistribution in testis in vivo. The electron dense particles found in the offspring seminiferous epithelium of all nano-TiO_2 recipient groups were confirmed to be the agglomerates around 200 nm by X-ray spectrometry under SEM and TEM. This analysis directly shows the localized position and number of the agglomerates. This suggested that even at the lowest dose, 0.5 μg of nano-TiO_2, it was possible to detect the distribution to the seminiferous epithelium. Regarding semi-quantification, agglomerate deposition in the testicular sections was correlated with nano-TiO_2 doses injected into pregnant mice (Fig. 2g). However, only small agglomerates of nano-TiO_2 below 200 nm were found in the offspring seminiferous epithelium of all recipient groups, independent from the injected dose during pregnancy. We have found the nano-TiO_2 translocation "in vivo" which agrees with the presumption from the experiment with ex vivo human placental perfusion (Wick et al. 2010), where nanomaterials with the diameter up to 240 nm cross the placental barrier. Similarly, rutile-type nano-TiO_2 (20.6 nm) retention in mouse lung following intratracheal instillation of 18, 54, and 162 μg/mouse was investigated using nanoscale hyperspectral microscopy. The hyperspectral mapping showed dose–dependent retention of nano-TiO_2 in the lung at up to 28 days post instillation. Several inflammatory mediators were shown to have changed in a dose- and time-dependent manner at both the mRNA and protein levels by DNA microarray analysis (Husain et al. 2013).

Generally, an ICP-MS is used to calculate the mass concentrations of nanoparticles in tissue. After examining the acute toxicity and biodistribution by ICP-MS, nano-TiO_2 have been found in the liver, kidneys, spleen, and lungs of adult mice after oral gavage administration of three sizes of anatase nano-TiO_2 (25, 80, and fine 155 ± 33 nm, 5 g/kg body weight). The 25 and 80 nm nanosized TiO_2 particles were shown to induce significant lesions in the liver and kidneys of female mice (Wang et al. 2007). On the other hand, nano-TiO_2 of both anatase and rutile forms (70/30) in the size range 20–30 nm administrated intravenously (at 5 mg/kg body weight) became decreasingly detectable over time in the liver, spleen, kidneys, and lungs of rats. It was concluded that nano-TiO_2 could be used safely in low doses due to the lack of any remarkable toxic health effects (Fabian et al. 2008).

The TEM observations reveal the failure of spermiation from Sertoli cells in all recipient groups. This may be caused by the biodistribution of nano-TiO_2 in seminiferous epithelium. This result was consistent with the investigations that nanoparticles exposure caused the toxicity on testicular function of totally different experiments (Hemmingsen et al. 2009) and (Kyjovska et al. 2013). Further studies are needed to evaluate biodistribution and effect of nano-TiO_2 exposure during pregnancy in more detail.

Conclusion

The average diameter (Z-average) of nano-TiO_2 prior to injection was increased in a dose–dependent manner; 1–1,000 μg/ml suspensions were from 193.3 ± 5.4 to 1980.3 ± 95.8 nm in diameter. The biodistribution in the testicular sections examined at 12 weeks postpartum were correlated between nano-TiO_2 doses injected to pregnant mice and the number of agglomerates in the testis by semi-quantitative evaluation. However, only small agglomerates of nano-TiO_2 below 200 nm transferred to the offspring after crossing the placental barrier, independent from the injected dose during

pregnancy. The failure of spermiation from Sertoli cells and elimination of abnormal spermatozoa were observed in all nano-TiO_2 recipient groups.

Acknowledgments This work was supported in part by a Grant-in-Aid for Science Research from the Ministry of Education, Culture, Sports, Science and Technology of Japan, a Grant-in Aid for the Private University Science Research Upgrade Promotion Business Academic Frontier Project, a grant of Strategic Research Foundation Grant-aided Project for Private Universities from Ministry of Education, Culture, Sport, Science, and Technology, and a Grant-in Aid for Health and Labour Sciences Research Grants, Research on Risk of Chemical Substances, from the Ministry of Health, Labour and Welfare".

References

Chen HH, Chien CC, Petibois C, Wang CL, Chu YS, Lai SF, Hua TE, Chen YY, Cai X, Kempson IM, Hwu Y, Margaritondo G (2011) Quantitative analysis of nanoparticle internalization in mammalian cells by high resolution X-ray microscopy. J Nanobiotechnol 9:14–28

De Jong WH, Hagens WI, Krystek P, Burger MC, Sips AJAM, Geertsma RE (2008) Particle size-dependent organ distribution of gold nanoparticles after intravenous administration. Biomaterials 29:1912–1919

Donaldson K, Stone V, Tran CL, Kreyling W, Borm PJA (2004) Nanotoxicology. Occup Environ Med 61:727–728

Fabian E, Landsiedel R, Ma-Hock L, Wiench K, Wohlleben W, van Ravenzwaay B (2008) Tissue distribution and toxicity of intravenously administered titanium dioxide nanoparticles in rats. Arch Toxicol 82(3):151–157

Hemmingsen JG, Hougaard KS, Talsnass C, Wellejus A, Loft S, Wallin H, Moller P (2009) Prenatal exposure to diesel exhaust particles and effect on the male reproductive system in mice. Toxicology 264:61–68

Husain M, Saber AT, Guo C, Jacobsen NR, Jensen KA, Yauk CL, Williams A, Vogel U, Wallin H, Halappanavar S (2013) Pulmonary instillation of low doses of titanium dioxide nanoparticles in mice leads to particle retention and gene expression changes in the absence of inflammation. Toxicol Appl Pharmacol 269(3):250–262

Komatsu T, Tabata M, Kubo-Irie M, Shimizu T, Suzuki K, Nihei Y, Takeda K (2008) The effects of nanoparticles on mouse testis Leydig cells in vitro. Toxicol In Vitro 22:1825–1831

Kyjovska ZO, Boisen AMZ, Jackson P, Wallin H, Vogel U, Hougaard KS (2013) Daily sperm production: application in studies of prenatal exposure to nanoparticles in mice. Reprod Toxicol 36:88–97

Mayhew TM, Muhlfeld C, Vanhecke D, Ochs M (2009) A review of recent methods for efficiently quantifying immunogold and other nanoparticles using TEM sections through cells, tissues and organs. Ann Anat 191:153–170

Maynard AD (2006) Safe handling of nanotechnology. Nature 444:267–269

Nel A, Xia T, Madler L, Li N (2006) Toxic potential of materials at the nanolevel. Science 311:622–627

Oberdorster G, Oberdorster E, Oberdorster J (2005) Nanotoxicology: an emerging discipline evolution from studies of ultrafine particles. Environ Health Perspect 113:823–839

Patri A, Umbreit T, Zheng J, Nagashima K, Goering P, Francke-Carroll S, Gordon E, Weaver J, Miller T, Sadrieh N, McNeil S, Stratmeyer M (2009) Energy dispersive X-ray analysis of titanium dioxide nanoparticle distribution after intravenous and subcutaneous injection in mice. J Appl Toxicol 29:662–672

Sharpe RM, Atanassova N, McKinnell C, Parte P, Turner KJ, Fisher JS, Kerr JB, Groome NP, Macpherson S, Millar MR, Saunders PTK (1998) Abnormalities in functional development of the Sertoli cells in rats treated neonatally with diethylstilbestrol: a possible role for estrogens in Sertoli cell development. Biol Reprod 59:1084–1094

Soto KF, Carrasco A, Powell TG, Garza KM, Murr LE (2005) Comparative in vitro cytotoxicity assessment of some manufactured nanoparticulate materials characterized by transmission electron microscopy. J Nanopart Res 7(2–3):145–169

Takeda K, Suzuki K, Ishihara A, Kubo-Irie M, Fujimoto R, Tabata M, Oshio S, Nihei Y, Ihara T, Sugamata M (2009) Nanoparticles transferred from pregnant mice to their offspring can damage the genital and cranial nerve systems. J Health Sci 55(1):95–102

Umbreit TH, Francke-Carroll S, Weaver JL, Miller TJ, Goering PL, Sadrieh N, Stratmeyer ME (2011) Tissue distribution and histopathological effects of titanium dioxide nanoparticles after intravenous or subcutaneous injection in mice. J Appl Toxicol 32:350–357

Wang J, Zhou G, Chen C, Yu H, Wang T, Ma Y, Jia G, Gao Y, Li B, Sun J, Li Y, Jiao F, Zhao Y, Chai Z (2007) Acute toxicity and biodistribution of different sized titanium dioxide particles in mice after oral administration. Toxicol Lett 168(2):176–185

Warheit DB, Sayes CM, Reed KLS, Swain KA (2008) Health effects related to nanoparticles exposures: environmental, health and safety considerations for assessing hazards and risks. Pharmacol Ther 120:35–42

Wick P, Malek A, Manser P, Meili D, Maeder-Althaus X, Diener L, Diener P-A, Zisch A, Krug H, Mandach U (2010) Barrier capacity of human placenta for nanosized materials. Environ Health Perspect 118:432–436

Yamashita K, Yoshioka Y, Higashisaka K, Mimura K, Morishita Y, Nozaki M, Yoshida T, Ogura T, Nabeshi H, Nagano H, Abe Y, Kamada H, Monobe Y, Imazawa T, Aoshima H, Shishido K, Kawai Y, Mayumi T, Tsunoda S, Itoh N, Yoshikawa T, Yanagihara I, Saito S, Tsutsumi Y (2011) Silica and titanium dioxide nanoparticles cause pregnancy complications in mice. Nat Nanotechnol 6(5):321–328

Yang H, Liu C, Yang D, Zhang H, Xi Z (2009) Comparative study of cytotoxicity, oxidative stress and genotoxicity induced by four typical nanomaterials: the role of particle size, shape and composition. J Appl Toxicol 29(1):69–78

Yoshida S, Hiyoshi K, Oshio S, Takano H, Takeda K (2010) Effect of fetal exposure to carbon nanoparticles on reproductive function in male offspring. Fertil Steril 93(5): 1695–1699

Colloids and Surfaces A: Physicochem. Eng. Aspects 442 (2014) 157–163

Contents lists available at ScienceDirect

Colloids and Surfaces A: Physicochemical and Engineering Aspects

journal homepage: www.elsevier.com/locate/colsurfa

Tunable plasma lipoprotein uptake/transport across the blood–brain barrier☆

Kenichiro Suzuki[a,b,*], Denis Adigüzel[b], Takanori Shinotsuka[a], Rei Ishibashi[a], Izumi Eguchi[a], Hideaki Oshima[a], Retsu Taniguchi[a], Stefan Thalhammer[b], Ken Takeda[a]

[a] Research Institute for Science & Technology, Tokyo University of Science, Chiba 278-8510, Japan
[b] Institute of Radiation Protection, Helmholtz Zentrum München, Neuherberg 85764, Germany

HIGHLIGHTS

- Biotechnological tools such as biocompatible nanoparticles have promising potential for theranostic strategies.
- Our study demonstrates the application of specifically constructed nanoparticles in the form of tunable plasma lipoproteins.
- Tuning of phosphatidylcholines and apolipoprotein B100 on nanoparticle surfaces is especially helpful for delivery route of glial precursor cells.

GRAPHICAL ABSTRACT

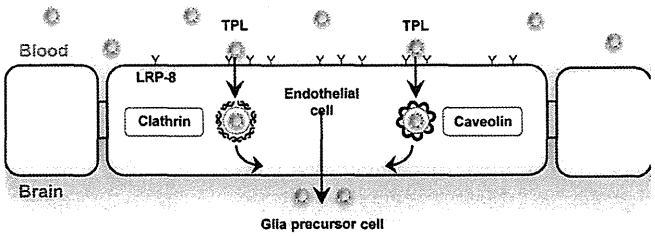

ARTICLE INFO

Article history:
Received 30 November 2012
Received in revised form 19 April 2013
Accepted 15 May 2013
Available online 29 May 2013

Keywords:
Apolipoprotein B100
Nanoparticle
Glia
Blood–brain barrier
Surfactant
Lipoprotein

ABSTRACT

Brain development and maintenance requires transportation of cerebral sustenance across the blood–brain barrier. Disorders of this process can induce neurodegenerative diseases, which can affect numerous patients and incur significant treatment expenses. Recent scientific advances suggest that knowledge of this transportation will lead to the development of tailor-made theranostic strategies. Biotechnological tools such as biocompatible nanoparticles have promising potential in this context, however, information about their consequences in the brain is largely unknown. The present study demonstrates the application of specifically constructed cerebral sustenance nanoparticles in the form of tunable plasma lipoproteins to provide information about their pathways to the brain and delivery to glia cells. Individual cell analysis in brain sections enabled us to understand the accumulation of tunable plasma lipoproteins in the cerebral cortex, striatum, and cerebellum, which have been previously identified as the incident regions of Alzheimer's disease, Parkinson's disease, and spinocerebellar ataxia. The adjustability of the tunable plasma lipoproteins enables their use in theranostic applications against neurodegenerative diseases.

© 2013 The Authors. Published by Elsevier B.V. All rights reserved.

☆ This is an open-access article distributed under the terms of the Creative Commons Attribution-NonCommercial-No Derivative Works License, which permits non-commercial use, distribution, and reproduction in any medium, provided the original author and source are credited.

* Corresponding author at: Research Institute for Science & Technology, Tokyo University of Science, 2641 Yamazaki, Noda-shi, Chiba 278-8510, Japan. Tel.: +81 4 7124 1501.
E-mail addresses: k_suzuki@rs.noda.tus.ac.jp, kenichiro-suzuki@i.softbank.jp (K. Suzuki).

0927-7757/$ – see front matter © 2013 The Authors. Published by Elsevier B.V. All rights reserved.
http://dx.doi.org/10.1016/j.colsurfa.2013.05.053

1. Introduction

The brain regulates mental and motor functions, which are based on neural networks. Neural network changes such as synaptogenesis, myelination, and neuro- and glio-genesis are associated with environmental factors and individual life events [1]. These changes are produced and preserved by cerebral sustenance transportation across the blood-brain barrier (BBB) [2]. It is generally known that glial cells such as astrocytes and oligodendrocytes play roles in brain development and maintenance [3]. They are not only relevant to the functions of synaptogenesis, myelination, and BBB, but are also involved in the pathogenesis of Alzheimer's disease (AD), Parkinson's disease (PD), and progressive spinocerebellar ataxia (SCA) [2,3]. In addition, it suggests that AD, PD, and SCA generation are induced by the loss of synapses and myelin or the malfunction of BBB in the brain [2,3]. Glial cells are responsible for the preservation of synapses, myelin, and BBB [2,3]. Therefore, innovation to achieve the aim of delivering drugs to glial cells will lead to key advancements in the development of effective theranostic methods [3,4]. However, the pathway from the plasma to glial cells for delivering drugs is as yet unknown.

Neurodegenerative diseases (NDs) such as AD, PD, and SCA are strongly associated with brain aging. These pathological phenotypes have been found in specific brain regions such as the cerebral cortex (AD), striatum (PD), and cerebellum (SCA) [5,6]. Clinical studies suggest that low vitamin A, D, and E levels in plasma contribute to AD, PD and SCA pathogenesis [5,6]. Since mammals are not able to synthesize essential substances such as fat-soluble vitamin A, D, and E, they must be extracted from their diet in the form of plant carotenes or animal retinyl esters, which are stored as retinoids in the liver following ingestion. These vitamins are subsequently transported by plasma lipoproteins (PLs) from the liver into the cardiovascular system [7,8]. But, incorporation of vitamin A, D, and E into PLs through retinol-binding proteins, vitamin D-binding proteins, and α-tocopherol transfer proteins are impaired in AD, PD, and SCA [5,6]. Moreover, it is widely accepted that vitamin A, D, and E are required for synaptogenesis, myelination, and glio-differentiation [9]. Consequently PLs that carry vitamins across the BBB could be vital for glial cells such as astrocytes and oligodendrocytes.

PL core consists mainly of triglycerides, (esterified) cholesterols, fat-soluble vitamins, fatty acids, and hormones, while the shell is composed of phospholipids, primarily phosphatidylcholines (PCs) and sphingomyelins, and apolipoproteins (Apos), such as Apo-A1-4, Apo-B48, Apo-B100, Apo-C1-3, ApoD, Apo-E2-4, and Apo-J [7,8]. PLs in plasma are found in high-density lipoproteins (HDLs), low-density lipoproteins (LDLs), intermediate-density lipoproteins (IDLs), very low-density lipoproteins (VLDLs), and chylomicrons. LDLs, IDLs, and VLDLs, which carry fat-soluble vitamins, mainly contain Apo-B100 [7,8]. Here, we hypothesize that PCs and Apo-B100 in LDLs would be targetor for glial cells. There is now evidence that glial cells highly express heparan sulfate proteoglycans and chondroitin sulfate proteoglycans, which can bind to LDLs [10,11]. Unfortunately, LDL pathway to glial cells has yet been uncharacterized.

In previous studies of brain delivery system, it has been shown that the modifications of nanoparticle surfaces are common approach to achieve novel drug therapies for delivering nanoparticles to the brain [12–15]. Actually, polysorbate 80 with Apo-B or Apo-E-mediated transport at the BBB has been demonstrated as targets for nanoparticle delivery to the brain [12]. However, it has been suggested that the polysorbate 80 induce toxic affects on the BBB permeability [12]. Therefore, future study for novel modification of nanoparticle surfaces should be focus on. Moreover, gold nanoparticles (AuNPs) are useful for the development of clinical applications and treatment strategies, since AuNPs are intended for practical use as contrast agents for an X-ray computed tomography (CT) [16–18].

Here our study demonstrates the application of specifically constructed cerebral sustenance nanoparticles in the form of tunable plasma lipoproteins (TPLs) in order to brain delivery system specifically targeting a subpopulation of glial cells.

2. Materials and methods

2.1. Preparation and characterization of tunable plasma lipoproteins

AuNPs of 20 nm diameter were produced by the Turkevich method [19] and were diluted to a final concentration of 500 μg/ml. PCs (850325P, Avanti Polar Lipids, USA) were dissolved by vortexing in distilled water (ppb level) to a concentration of 1 mg/ml at 37 °C. Aggregates were removed by filtration through a 100 nm cutoff filter (SLVV033RS, Millipore, USA). A 400 μl aliquot of the resulting solution was added to 100 μl of the AuNPs. The AuNPs were coated with the PCs by stirring overnight at 37 °C. The sizes and shapes of the resulting TPLs were determined via transmission electron microscopy (TEM) (JEM-1200 EXII, JEOL, Japan) with negative staining with uranyl acetates. The cell tracker, CM-DiI (DiI) (C7000, Molecular Probes™, USA), was added at a rate of 0.5 μl per 500 μl of distilled water from a 1 mg/ml stock solution in DMSO. Next, 500 μl of the diluted DiI-solution was mixed with 500 μl of the PC-coated AuNPs by gentle stirring, followed by incubation at 37 °C for 30 min inside a sealed tube. Finally, 1 ml of 1 μg/ml Apo-B100 (A5353, Sigma, USA) in saline was added to 1 ml of the DiI-labeled PC-coated AuNPs and incubated for 3 h at 37 °C. The TPLs were re-dispersed in saline and residual PC, Apo, and DMSO solvent were removed by centrifuging twice at 20,000 × g for 5 min. Remaining aggregates were removed by filtration using a 100 nm cutoff filter. Both their hydrodynamic diameter and their PDI were determined by DLS measurements (Nano-ZS, Sysmex, Netherlands). Particle number data (%) were obtained from distribution analyses of the non-negative linear least squares method.

2.2. In vitro experiments

Endothelial cells (ECs) (bEnd.3, ATCC, USA) from mouse brains were cultured in cell culture medium (DMEM, Wako, Japan), supplemented with 10% heat-inactivated fetal bovine serum (Bio West, France) and 0.1% gentamycin (Sigma–Aldrich, USA). Incubation was carried out at 37 °C in a humidified atmosphere of 5% CO_2. The ECs were seeded to a density of 0.7×10^4 cells/cm^2 onto glass plates (1.1 cm^2) that were coated with rat-tail collagen to a density of 5 μg/cm^2 inside flat bottom 24-well plates (area: 1.55 × 1.55 cm^2, height: 1.75 cm). ECs that grew to sub-confluence, corresponding to final cell densities of 2.5×10^4 cells/cm^2, were treated with TPL for different incubation times (6 and 12 h). 100 μl of TPL were added to 900 μl of the cell medium to achieve a final concentration of 2.5 μg/ml. The TPL-containing cell culture medium was replaced with non-TPL-enriched cell medium 30 min after the end of the 12 h incubation. The ECs were then washed twice with PBS and fixed with 4% paraformaldehyde. For the immunocytochemical analyses, ECs were blocked with 3% goat serum for 20 min and were incubated overnight with primary antibodies to clathrin HC H-300 (sc-9069, Santa Cruz Biotechnology, USA), caveolin-1 (C-term), LRP8, and LDL receptor (C-term) (1249-1, 3156-1, and 1956-1, Epitomics Inc., USA) at 4 °C. They were subsequently incubated with secondary antibodies: Alexa Fluor®

488 goat anti-rabbit IgG (A11034, Molecular probes, USA) and their nuclei were stained using H33342 (B2261, Sigma–Aldrich, USA). Cell imaging was achieved using a confocal microscope (Leica SP-II, Leica, Germany) with a 63× oil immersion objective. Endothelial cell vesicle with internalized TPL was determined via TEM.

2.3. In vivo experiments

100 μl of 12.5 or 250 μg/ml saline-diluted TPLs were tail-vein-injected into C57BL/6J mice. After 24 h they were killed by an intraperitoneal injection of pentobarbital diluted in saline and perfused via the heart with 2–5 ml of 0.01 M PBS and 4% paraformaldehyde. The flow rate was 1 ml/min. The brains were removed and fixed with 4% paraformaldehyde in PBS for 2 days. After dehydration in 5% sucrose, the samples were sectioned to a thickness of 10 μm along the sagittal surfaces using a microtome (LS-113, Yamato, Japan). Serial sections were cut from the interaural side of the mouse brain. For immunohistochemical analyses of the brain, the sections were incubated overnight with the primary rabbit polyclonal anti-Olig2 antibody (AB9610, Millipore, USA) at 4 °C. Subsequently, the sections were incubated with secondary antibodies: Alexa Fluor® 488 chicken anti-rabbit IgG (A21441, Molecular probes, USA). Brain ECs were stained using FITC-conjugated TOMATO lectin (FL-1171, Vector Laboratories, USA). The cell nuclei were stained using H33342. The fluorescent signals from Olig2 and TPLs in the brain sections were analyzed by fluorescence microscopy (BZ-9000, KEYENCE, Japan) with a Plan Apo 20×/0.75 DIC N2 objective lens.

2.4. Statistical analysis

Statistical significance was determined by Student's *t*-test (Fig. 2B andSupplementary Fig. 2B) and Tukey's test (Fig. 3C). Differences were considered significant with a *P* value; $^{*}P < 0.005$ by Student's *t*-test, $^{*}P < 0.05$ by Tukey's test.

Supplementary data associated with this article can be found, in the online version, at http://dx.doi.org/10.1016/j.colsurfa.2013.05.053.

3. Results and discussion

3.1. Development of tunable plasma lipoproteins

The structure of PLs and the self-assembly processes of TPLs are depicted in Fig. 1A. The term "tunable" is used to refer to refinement in terms of size and shape, phospholipid and protein coating, or delivery routes. To synthesize the TPLs, AuNPs were used to assemble the TPL cores. AuNPs have negative charges at the hydrophobic surfaces. This AuNP behaves likes a hydrophobic solution, and therefore constitutes an aqueous dispersion of insoluble solid particles [20]. AuNPs were then functionalized with biomolecules containing PCs and Apo-B100, which are common components of LDLs [8]. The synthesis was based on a self-assembly

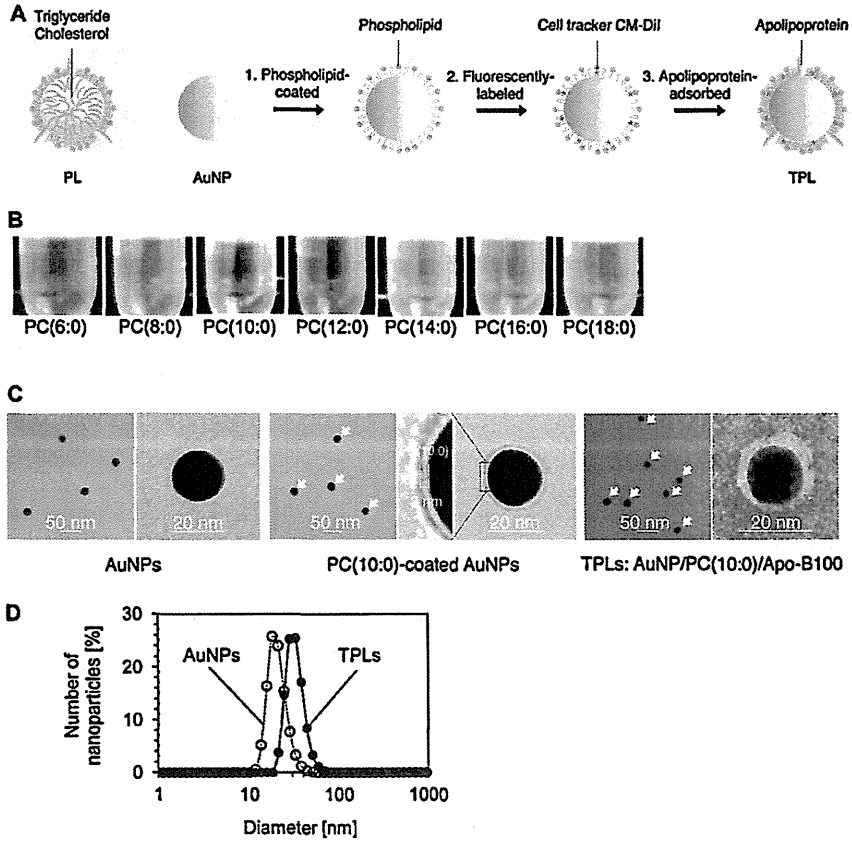

Fig. 1. Preparation and characterization of tunable plasma lipoproteins. (A) The schematic illustration of plasma lipoproteins (PLs) and the schematic depiction of the self-assembly steps involved in the production process of tunable plasma lipoproteins (TPLs). Gold nanoparticles (AuNPs) were (1) coated with phosphatidylcholines (PCs) and (2) labeled with the cell tracker CM-DiI for fluorescent imaging. Finally, (3) apolipoprotein-B100 were added. (B) Images of TPL-solutions produced by PCs with different lengths of saturated fatty acid hydrocarbon chains (6:0, 8:0, 10:0, 12:0, 14:0, 16:0, and 18:0). Red color indicates that TPLs are dispersed in saline. (C) Transmission electron micrographs of AuNPs, PC(10:0)-coated AuNPs, and TPLs: AuNP/PC(10:0)/Apo-B100. Arrows show the PCs (10:0) and Apo-B100. The coated layer is visible as a bright contrast at the particle surface. The PC layer thickness is 3 nm (see a magnified view). (D) Hydrodynamic particle diameters of AuNPs in water and TPLs in saline.

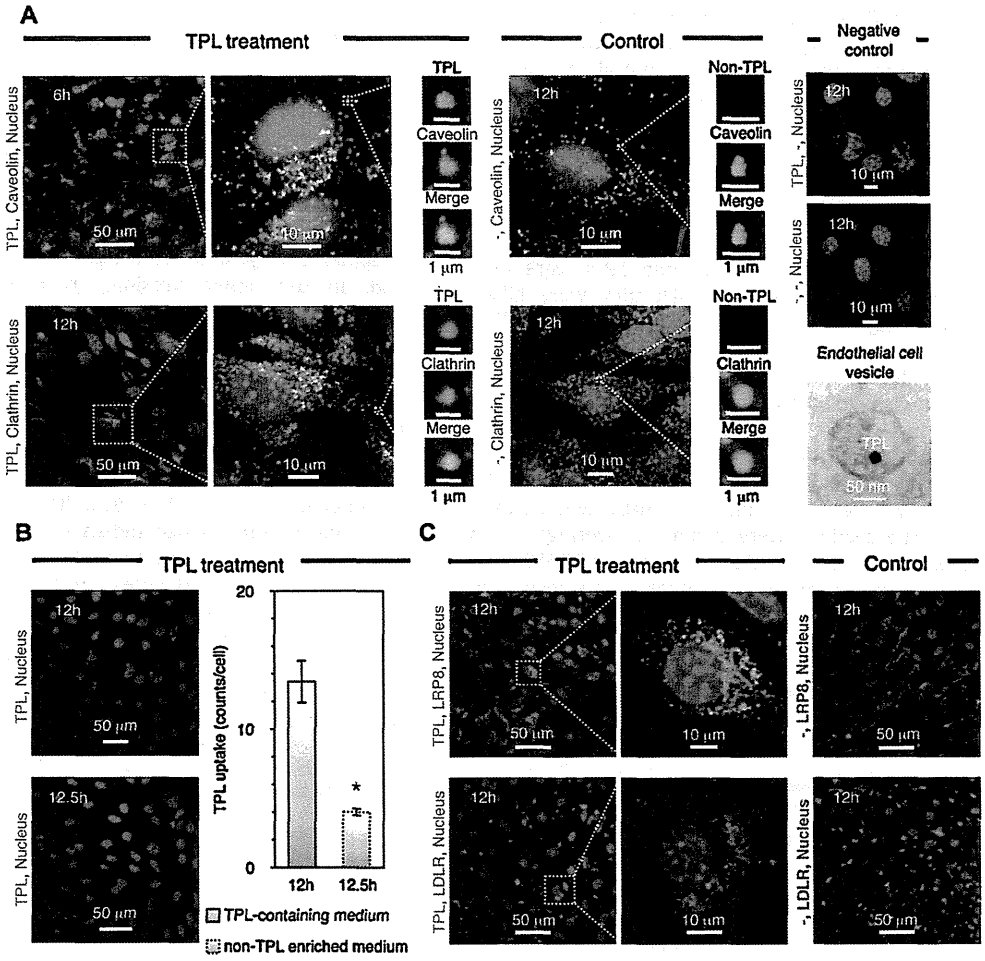

Fig. 2. Analyses of tunable plasma lipoproteins internalized into endothelial cells. (A) Confocal microscopy images of clathrin- and caveolin-coated vesicles in endothelial cells (ECs) incubated with tunable plasma lipoproteins (TPLs) and saline (control). Green (λ_{Ex} = 495 nm, λ_{Em} = 519 nm for Alexa Fluor® 488) indicates clathrin and caveolin. Red signals (λ_{Ex} = 553 nm, λ_{Em} = 570 nm for cell tracker CM-DiI) correspond to TPLs. The nuclei in the ECs are stained using H33342 (blue color: λ_{Ex} = 355 nm, λ_{Em} = 465 nm). Merged color (yellow) indicates that clathrin and caveolin were colocalized with TPLs. Negative controls indicate that green and red signals are not due to background. Transmission electron micrographs of an endothelial cell vesicle with internalized TPL. (B) TPL uptake after replacement of TPL-containing cell culture medium with non-TPL-enriched cell medium after 12 h of incubation. Clearly visible is a decrease in the previously internalized TPL in the EC after 30 min. Estimations of the amount of TPL uptake into ECs were performed by confocal microscopy. Each data point represents the mean ± S.E. of n = 5 images (237 μm × 237 μm). *P < 0.005 by Student's t-test. (C) Confocal microscopy images of low-density lipoprotein receptor-related protein 8 (LRP8) and low-density lipoprotein receptor (LDLR) in ECs incubated with TPLs. Green (λ_{Ex} = 495 nm, λ_{Em} = 519 nm for Alexa Fluor® 488) indicates LRP8 and LDLR. Red signals indicate TPLs. The EC nuclei were stained using H33342.

process. PCs with different lengths of saturated fatty acid hydrocarbon chains (6:0, 8:0, 10:0, 12:0, 14:0, 16:0, and 18:0) were investigated. PCs (10:0 and 12:0) adsorbed solely to AuNP surfaces, which additionally increased their dispersion rate in saline (shown in Fig. 1B). However, PCs (6:0, 8:0, 14:0, 16:0, and 18:0) were insufficiently adsorbed at AuNP surfaces, and PC-uncoated AuNPs were aggregated in saline. This phenomenon can be understood from the solubility (known as critical micelle concentration) of PCs with different lengths of saturated fatty acid hydrocarbon chains (6:0–18:0). By comparison, the PCs (14:0–18:0) were not dispersed in an aqueous solution due to their low solubility. Alternatively, PCs (6:0 and 8:0) were not adsorbed at AuNP surfaces due to their high solubility. This factor contributes to their self-assembly process. As shown in Fig. 1C, AuNPs, PC(10:0)-coated AuNPs, and TPLs: AuNP/PC(10:0)/Apo-B100 were observed by TEM. These results indicate that the AuNP surfaces are coated by PCs (10:0) and Apo-B100. The surface coverage of Apo-B100 adsorbed to the PC(10:0)-coated AuNPs was 96 ± 3.1% (n = 63 particle). Dynamic light scattering (DLS) analyses were used to confirm hydrodynamic particle diameter of AuNPs and TPLs. The hydrodynamic particle diameters were 19 ± 1 nm at 0.27% Polydispersity index (PDI) (AuNPs in water) and 30 ± 2 nm at 0.44% PDI (TPLs in saline), as shown in Fig. 1D. This result indicates that TPLs are stable in saline. Additionally, phosphatidylglycerols (PG) (10:0, 12:0, 14:0, 16:0, and 18:0), phosphatidic acids (PA) (6:0, 8:0, 10:0, 12:0, 14:0, and 16:0), and phosphatidylserine (PS) (8:0, 10:0, 12:0, 14:0, and 16:0) were investigated. Consequently, PA(10:0)-, PS(14:0)-, and PG(16:0)-coated AuNPs are observed (Supplementary Fig. 1A). AuNP/PC(10:0)/Apo-A1 and AuNP/PC(10:0)/Apo-E4 were also produced and characterized (Supplementary Fig. 1B). Thus, we developed a specific nanotechnique for TPL-preparation that is based on a self-assembly process.

Supplementary data associated with this article can be found, in the online version, at http://dx.doi.org/10.1016/j.colsurfa.2013.05.053.

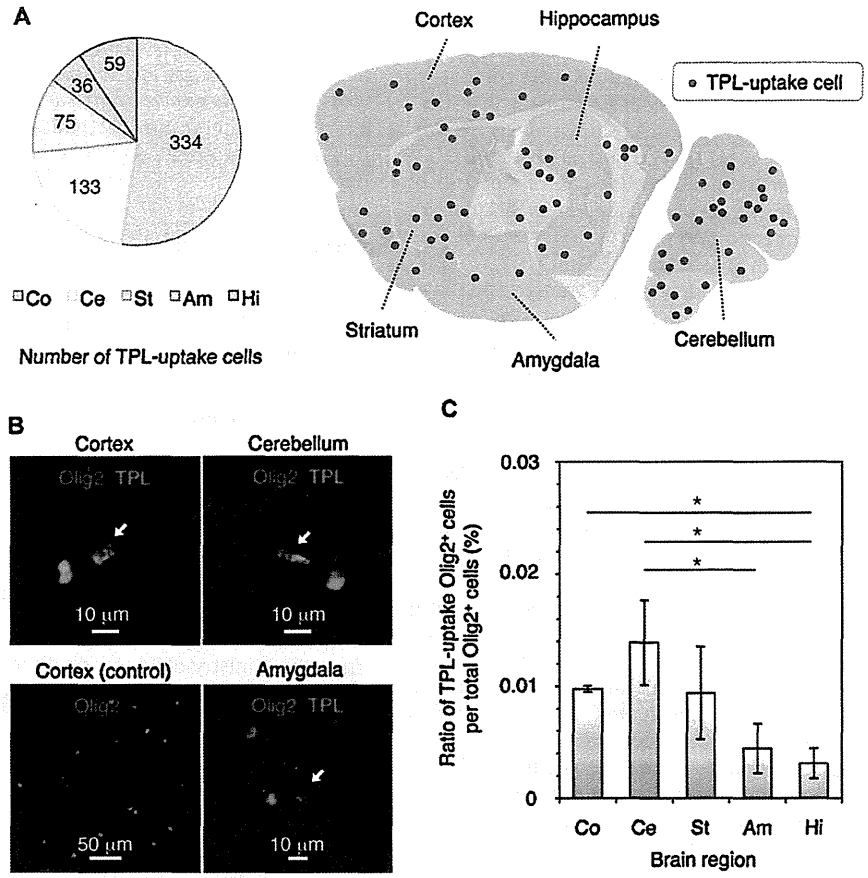

Fig. 3. Analyses of tunable plasma lipoproteins in the brain. (A) Pie graph showing the number of cells in the brain with TPL-uptake (cortex: Co, cerebellum: Ce, striatum: St, amygdala: Am, and hippocampus: Hi). Schematic of the mouse brain showing localized TPL; width of 360 μm. (B) Fluorescent microscopy images of TPL-uptake cells that expressed oligodendrocyte transcription factor2 (Olig2). Green (λ_{Ex} = 495 nm, λ_{Em} = 519 nm for Alexa Fluor® 488) represents Olig2. Red signals indicate TPLs labeled with the cell tracker, CM-DiI (λ_{Ex} = 553 nm, λ_{Em} = 570 nm). Arrows show the TPL-uptake Olig2$^+$ cells. In order to analyze the fluorescent signals of TPL uptake cells while reducing intrinsic fluorescent signals we make a 10 μm section. At this thickness it is usually only possible to find one TPL uptake cell within a section. With a thicker section we would be less likely to be able to detect TPLs. Thus, it is only possible to produce an image of a single cell. (C) Ratio of TPL uptake into Olig2$^+$ cells per total Olig2$^+$ cells in different regions of the brain (cortex: Co, cerebellum: Ce, striatum: St, amygdala: Am, and hippocampus: Hi). Asterisk indicates there were larger numbers of TPL-uptake Olig2$^+$ cells in the cerebellum than the amygdala and hippocampus, and in the cortex than the hippocampus. Each data point represents the mean ± S.D. of n = 3 mice (100 serial sagittal sections per mouse). *P < 0.05 by Tukey's test.

3.2. *Internalization of tunable plasma lipoproteins in endothelial cells*

The transcytotic pathway of TPL: AuNP/PC(10:0)/Apo-B100 into endothelial cells (ECs) was elucidated in vitro with caveolin-coated vesicles (CAVs) and clathrin-coated vesicles (CLVs), which are capable of mediating transcytosis from blood to the brain [21]. Immunocytochemical analyses (Fig. 2A) revealed the internalization of TPLs at the incubation times of 6 h (caveolin images) and 12 h (clathrin images). Additionally, confocal microscopy images of control (without TPLs) and negative control (without antibodies or without TPLs and antibodies) are shown. A TEM image of TPL-including example of intracellular vesicle was observed. To analyze the uptake and efflux of TPLs in the ECs, total intensity of the DiI-signals from TPLs that internalized into the ECs were quantified. ECs that grew to sub-confluence were treated with TPLs with a final mass concentration of 2.5 μg/ml cell culture medium for 12 h. The TPL-containing cell culture medium was replaced with non-TPL-enriched cell medium after 12 h of incubation. As shown in Fig. 2C, we found a reduction in the quantity of TPLs to 70% after 30 min. This result indicates that CAVs and CLVs in ECs play a role as frequent uptake and efflux carriers for TPLs. Low-density lipoprotein receptor-related protein 8 (LRP8) and low-density lipoprotein receptor (LDLR) were investigated to identify a receptor that could be associated with TPLs in the ECs. It is generally known that LRP8 and LDLR are required for endocytosis of LDLs [22,23]. Moreover, LRP8 is localized in CAVs, gene expression of LRP8 in mouse brain ECs is higher than LRP1, LRP2, and LDLR, and LRP8 in mouse brain ECs is enriched in comparison to LRP8 in liver or lung ECs [23,24]. Consequently, we chose the LRP8 and LDLR in established brain endothelial cell line (bEnd.3 cells). From the observations of LRP8 and LDLR in ECs, TPLs were recognized by LRP8 but not LDLR (Fig. 2E). Hence, TPLs could acquire an EC recognition ability in the same way as PLs by the tuning of PL components on the AuNP surfaces. Additionally, AuNP/PC(10:0)/Apo-A1 and AuNP/PC(10:0)/Apo-E4 were also elucidated in vitro. Consequently we found that they internalized into ECs via the CAVs and CLVs (Supplementary Fig. 2A). A reduced quantity of AuNP/PC(10:0)/Apo-A1 to 63% and AuNP/PC(10:0)/Apo-E4 to 78% were also shown (Supplementary Fig. 2B). These results indicate that both Apo-A1 and Apo-E4 have similar characteristics to Apo-B100 for the internalization of TPLs into ECs.

3.3. *The brain cell specificity of tunable plasma lipoproteins*

To confirm transportation of TPL: AuNP/PC(10:0)/Apo-B100 across the BBB, counts of cells which had successfully taken-up TPLs (TPL-uptake cells) were obtained in serial sagittal brain sections at

a thickness of 10 μm. Using a Plan Apo 20× objective lens, the optical fields were scanned in all areas of the brain sections. The DiI induced fluorescent signals of TPLs in the sections were compared to saline injected sections and distinguished from the intrinsic fluorescent signals (Supplementary Fig. 3A). As shown in Fig. 3A, we found TPL-uptake cells in the cortex (334 cells), the cerebellum (133 cells), striatum (75 cells), amygdala (36 cells), and hippocampus (59 cells) from the observation of whole brain sections (895 pieces) treated with a 12.5 μg TPL injection. Additionally TPL-accumulated regions with a width of 360 μm are shown. To identify the types of neural cells, we examined the oligodendrocyte transcription factor 2 (Olig2) in TPL-uptake cells using an immunohistochemical analysis. Olig2, which is the basic helix-loop-helix transcription factor, is essential for specification and maturation of astrocytes and oligodendrocytes [25–27]. Olig2$^+$ cells are defined as immature oligodendrocyte precursor cells (OPCs) (also known as NG2 cells) [25–27]. From the analyses of 100 serial sagittal sections, we found TPL-uptake cells (102 cells), 54% of which were identified as Olig2$^+$ cells, and 42% of which were identified as brain-ECs (Fig. 3B and Supplementary Fig. 3B). The brain ECs were shown using staining by FITC-conjugated TOMATO lectin (a known endothelial cell marker). Fluorescent images of Olig2$^+$ cells (without TPLs) in the cortex are shown (control). Moreover, Fig. 3C shows there were larger numbers of TPL-uptake Olig2$^+$ cells in the cerebellum than the amygdala and hippocampus, and in the cortex than the hippocampus at the 25 μg TPL injection amount (100 serial sagittal sections per mouse, $n = 3$ mice). Although we found low numbers of TPL-uptake Olig2$^+$ cells (Fig. 3C), this finding would be explained by the comparison of TPLs with LDLs. In fact, the TPL-injected mass (M) of 25 μg was used. However, the naturally occurring LDL mass (M) was 135 μg in 5 week-old mouse plasma (exact LDL mass was adapted from [28]). Hence, total particle numbers (N) of TPLs and LDLs can be calculated as follows:

$$N = \frac{M}{\rho V}$$

where V is the volume per a TPL (particle diameter: 30 nm) and an LDL (particle diameter: 21–27 nm), ρ is the density of a TPL (19.32 g/cm^3: gold) or an LDL (1.019–1.063 g/cm^3). Calculated data show that total particle numbers of TPLs (particle number: 9.2×10^{10} counts) were 200 times lower compared with those of LDLs (particle number: 1.9×10^{13} counts). Therefore, this analysis enabled us to calculate the mean for low numbers of TPL-uptake Olig2$^+$ cells. Therefore, our study is the first evidence that tuning of PCs and Apo-B100 on nanoparticle surfaces is especially helpful for delivery route of glial cell.

Supplementary data associated with this article can be found, in the online version, at http://dx.doi.org/10.1016/j.colsurfa.2013.05.053.

4. Conclusions

Malfunction of glial cells is a serious risk factor for NDs like AD, PD, and SCA generation and should be targeted for therapeutic intervention. At present, it is difficult to adequately treat these diseases with clinical therapies and medication. Nanoparticles will enhance and enable novel possibilities in the research area of medicine. We constructed specific TPLs and clearly demonstrated their pathways to the brain and delivery to glia cells. Our results show that TPL-accumulations occur especially in AD, PD, and SCA generation regions in the brain. Hence, these findings offer the potential to specifically control regions of ND generation. Furthermore, glial cells, which had taken-up TPLs, may relate to brain self-organizing processes (BSOPs), which are produced and preserved by cerebral sustenance transportation across the BBB. TPLs may help to fight AD, PD, and SCA by elucidation of the link between TPLs and BSOPs, since AuNPs, which are used to assemble the TPL cores, are attractive as a contrast agent for X-ray CT-imaging. We expect that investigations into the adjustment or tuning of TPLs will lead to key advances for human applications in the development of effective ND theranostic methods, improve monitoring and analysis of glial cells, and allow access to innovative neurobiological information.

Author contributions

K.S. and D.A. led the experimental design. K.S., T.S., R.I., I.E., H.O., and R.T. performed the experiments. K.S., D.A., S.T., and K.T. discussed data evaluation. K.S. and D.A. wrote the paper.

Competing financial interests

The authors declare no competing financial interests.

Acknowledgements

The authors thank R. Niki and S. Yanagida for expert technical assistance in animal treatment and immunohistochemical analysis. This work was supported by a Grant-in-Aid for Science Research from the Ministry of Education, Culture, Sports, Science and Technology of Japan and a Grant-in Aid for Health and Labor Sciences Research Grants from the Ministry of Health, Labor and Welfare of Japan.

References

[1] H. van Praag, G. Kempermann, F.H. Gage, Neural consequences of environmental enrichment, Nat. Rev. Neurosci. 1 (2000) 191–198.
[2] N.J. Abbott, L. Rönnbäck, E. Hansson, Astrocyte-endothelial interactions at the blood–brain barrier, Nat. Rev. Neurosci. 7 (2006) 41–53.
[3] B.A. Barres, The mystery and magic of glia: a perspective on their roles in health and disease, Neuron 60 (2008) 430–440.
[4] R.J.M. Franklin, C. Ffrench-Constant, Remyelination in the CNS: from biology to therapy, Nat. Rev. Neurosci. 9 (2008) 839–855.
[5] M. Maden, Retinoic acid in the development regeneration and maintenance of the nervous system, Nat. Rev. Neurosci. 8 (2007) 755–765.
[6] F. Taroni, S. DiDonato, Pathways to motor incoordination: the inherited ataxias, Nat. Rev. Neurosci. 5 (2004) 641–655.
[7] H.J. Kayden, M.G. Traber, Absorption lipoprotein transport, and regulation of plasma concentrations of vitamin E in humans, J. Lipid Res. 34 (1993) 343–358.
[8] R.W. Mahley, T.L. Innerarity, Lipoprotein receptors and cholesterol homeostasis, Biochim. Biophys. Acta 737 (1983) 197–222.
[9] B.A. Barres, M.A. Lazar, M.C. Raff, A novel role for thyroid hormone glucocorticoids and retinoic acid in timing oligodendrocyte development, Development 120 (1994) 1097–1108.
[10] J.D. Cahoy, B. Emery, A. Kaushal, L.C. Foo, J.L. Zamanian, K.S. Christopherson, Y. Xing, J.L. Lubischer, P.A. Krieg, S.A. Krupenko, W.J. Thompson, B.A. Barres, A transcriptome database for astrocytes neurons, and oligodendrocytes: a new resource for understanding brain development and function, J. Neurosci. 28 (2008) 264–278.
[11] K. Lipponen, P.W. Stege, G. Cilpa, J. Samuelsson, T. Fornstedt, M.-L. Riekkola, Three different approaches for the clarification of the interactions between lipoproteins and chondroitin-6-sulfate, Anal. Chem. 83 (2011) 6040–6046.
[12] J. Kreuter, Nanoparticlate systems for brain delivery of drugs, Adv. Drug. Delivery. Rev. 47 (2001) 65–81.
[13] J. Kreuter, D. Shamenkov, V. Petrov, P. Ramge, K. Cychutek, C. Koch-brandt, R. Alyautdin, Apolipoprotein-mediated transport of nanoparticle-bound drugs across the blood–brain barrier, J. Drug Target. 10 (2002) 317–325.
[14] D. Begley, Delivery of therapeutic agents to the central nervous system: the problem and the possibilities, Pharm. Ther. 104 (2004) 29–45.
[15] A. Zensi, D. Begley, C. Pontikis, C. Legros, L. Mihoreanu, S. Wagner, C. Büchel, H. von Briesen, J. Kreuter, Albumin nanoparticles targeted with Apo E enter the CNS by transcytosis and are delivered to neurons, J. Control. Release 137 (2009) 78–86.
[16] D.P. Cormode, T. Skajaa, M.M. van Schooneveld, R. Koole, P. Jarzyna, M.E. Lobatto, C. Calcagno, A. Barazza, R.E. Gordon, P. Zanzonico, E.A. Fisher, Z.A. Fayad, W.J.M. Mulder, Nanocrystal core high-density lipoproteins: a multimodality contrast agent platform, Nano Lett. 8 (2008) 3715–3723.
[17] D.P. Cormode, E. Roessl, A. Thran, T. Skajaa, R.E. Gordon, J. Schlomka, V. Fuster, E.A. Fisher, W.J.M. Mulder, R. Proksa, Z.A. Fayad, Atherosclerotic plaque

composition: analysis with multicolor CT and targeted gold nanoparticles, Radiology 256 (2010) 774–782.
[18] B.Y.S. Kim, J.T. Rutka, W.C.W. Chan, Nanomedicine, N. Engl. J. Med. 363 (2010) 2434–2443.
[19] G. Frens, Controlled nucleation for the regulation of the particle size in monodisperse gold suspensions, Nature 241 (1973) 20–22.
[20] S.L. Goodman, G.M. Hodges, D.C. Livingston, A review of the colloidal gold marker system, Scan. Electron Microsc. 11 (1980) 133–146.
[21] F. Hervé, N. Ghinea, J. Scherrmann, CNS delivery via adsorptive transcytosis, AAPS. J. 10 (2008) 455–472.
[22] W.J. Schneider, J. Nimpf, LDL receptor relatives at the crossroad of endocytosis and signaling, Cell. Mol. Life Sci. 60 (2003) 892–903.
[23] D.R. Riddell, X.M. Sun, A.K. Stannard, A.K. Soutar, J.S. Owen, Localization of apolipoprotein E receptor 2 to caveolae in the plasma membrane, J. Lipid Res. 42 (2001) 998–1002.
[24] R. Daneman, L. Zhou, D. Agalliu, J.D. Cahoy, A. Kaushal, B.A. Barres, The mouse blood–brain barrier transcriptome: a new resource for understanding the development and function of brain endothelial cells, PLoS One 5 (2010) e13741.
[25] C.A. Marshall, B.G. Novitch, J.E. Goldman, Olig2 directs astrocyte and oligodendrocyte formation in postnatal subventricular zone cells, J. Neurosci. 25 (2005) 7289–7298.
[26] J. Cai, Y. Chen, W.H. Cai, E.C. Hurlock, H. Wu, S.G. Kernie, L.F. Parada, Q.R. Lu, A crucial role for olig2 in white matter astrocyte development, Development 134 (2007) 1887–1899.
[27] X. Zhu, H. Zuo, B.J. Maher, D.R. Serwanski, J.J. LoTurco, Q.R. Lu, A. Nishiyama, Olig2-dependent developmental fate switch of NG2 cells, Development 139 (2012) 2299–2309.
[28] S. Qiu, N. Bergeron, L. Kotite, R.M. Krauss, A. Bensadoun, R.J. Havel, Metabolism of lipoproteins containing apolipoprotein B in hepatic lipase-deficient mice, J. Lipid Res. 39 (1998) 1661–1668.

Umezawa et al. Particle and Fibre Toxicology 2013, 10:64
http://www.particleandfibretoxicology.com/content/10/1/64

PARTICLE AND FIBRE TOXICOLOGY

RESEARCH Open Access

Effect of aerosol particles generated by ultrasonic humidifiers on the lung in mouse

Masakazu Umezawa[1,2*†], Keisuke Sekita[1†], Ken-ichiro Suzuki[2], Miyoko Kubo-Irie[2], Rikio Niki[2], Tomomi Ihara[3], Masao Sugamata[3] and Ken Takeda[1,2]

Abstract

Background: Ultrasonic humidifiers silently generate water droplets as a cool fog and produce most of the dissolved minerals in the fog in the form of an aerosolized "white dust." However, the health effect of these airborne particles is largely unknown. This study aimed to characterize the aerosol particles generated by ultrasonic humidifiers and to investigate their effect on the lung tissue of mice.

Methods: An ultrasonic humidifier was operated with tap water, high-silica water, ultrapure water, or other water types. In a chamber (0.765 m^3, ventilation ratio 11.5 m^3/hr), male ICR mice (10-week-old) were exposed by inhalation to an aerosol-containing vapor generated by the humidifier. After exposure for 7 or 14 days, lung tissues and bronchoalveolar lavage fluid (BALF) were collected from each mouse and examined by microarray, quantitative reverse transcription-polymerase chain reaction, and light and electron microscopy.

Results: Particles generated from the humidifier operated with tap water had a mass concentration of 0.46 ± 0.03 mg/m^3, number concentration of $(5.0 \pm 1.1) \times 10^4$/$cm^3$, and peak size distribution of 183 nm. The particles were phagocytosed by alveolar macrophages in the lung of mice. Inhalation of particles caused dysregulation of genes related to mitosis, cell adhesion molecules, MHC molecules and endocytosis, but did not induce any signs of inflammation or tissue injury in the lung.

Conclusion: These results indicate that aerosol particles released from ultrasonic humidifiers operated with tap water initiated a cellular response but did not cause severe acute inflammation in pulmonary tissue. Additionally, high mineral content tap water is not recommended and de-mineralized water should be recommended in order to exclude any adverse effects.

Background

The indoor air environment is important for human health because humans spend most of their time indoors [1]. Volatile organic compounds [2], microorganisms [3], environmental allergens [4], and particle matter [5] have been reported as important factors of the indoor environment. It is necessary to conduct safety assessments of consumer products, e.g., air conditioners, humidifiers, and air purifiers, which are all prevalent in commercial facilities, hospitals, schools, and homes.

The most important factors of the indoor air environment are temperature and humidity [6,7]. Humidifiers are used to prevent excessive drying and to maintain comfortable room humidity. There are three types of humidifier: evaporative, steam, and ultrasonic vaporizers [8]. While ultrasonic humidifiers need little electricity to work and release cooler vapor than the steam-type, they must be cleaned to avoid bacterial contamination since the vapor contains all impurities that are present in the reservoir [9,10]. Only ultrasonic humidifiers release most of the dissolved and suspended components of the water, including microorganisms and pathogens, into the air [11]. Fatal pulmonary damage, i.e., rapidly progressive respiratory fibrosis, has also been reported when a water aerosol which contained biocides was released from humidifiers and was inhaled by humans [12].

* Correspondence: masa-ume@rs.noda.tus.ac.jp
†Equal contributors
[1]Department of Hygienic Chemistry, Faculty of Pharmaceutical Sciences, Tokyo University of Science, 2641 Yamazaki, Noda, Chiba 278-8510, Japan
[2]The Center for Environmental Health Science for the Next Generation, Research Institute for Science and Technology, Tokyo University of Science, 2641 Yamazaki, Noda, Chiba 278-8510, Japan
Full list of author information is available at the end of the article

BioMed Central

© 2013 Umezawa et al.; licensee BioMed Central Ltd. This is an open access article distributed under the terms of the Creative Commons Attribution License (http://creativecommons.org/licenses/by/2.0), which permits unrestricted use, distribution, and reproduction in any medium, provided the original work is properly cited.

Even if the water has no contamination by microorganisms or pathogens, ultrasonic humidifiers may exert some effects on human health. Previous studies showed that ultrasonic humidifiers may release dissolved minerals as an aerosol [13]. Highsmith et al. [14] reported that the fine particle concentration exceeded 6.3 mg/m^3 when an ultrasonic humidifier was operated in a closed room. A subsequent study reported that the "white dust" induced lung injury [15]. However, the detailed components of the aerosol (or dust) and its health effect (e.g., inflammatory response in the lung) remained unknown. The aim of the present study was to characterize the aerosol particles generated by an ultrasonic humidifier and to investigate their effects on the lung in a mouse model.

Methods

Ultrasonic humidifier operation

An ultrasonic humidifier, BBH-07 (Hanwa Ltd., Osaka, Japan) was placed in each chamber with a volume of 0.765 m^3 and a ventilation ratio of 11.5 m^3/hr in the Center for Environmental Health Science for the Next Generation (Research Institute for Science and Technology, Tokyo University of Science, Noda, Chiba, Japan). The humidifier was operated at approximately 60 mL/hr liquid output rate with one of the following types of water: tap water obtained in Noda-city (Chiba, Japan), high-silica water purchased from Riken Mineral Kenkyusho K.K (Ebino, Miyazaki, Japan), a graded series of calcium chloride solution (4–400 mg/L of calcium), reverse osmotic membrane-filtration water (RO water) purchased from Ako Kasei Co., Ltd. (Ako, Hyogo, Japan), or an ultrapure water generated by an Automatic Sanitization Module (Merck Millipore, Billerica, MA, USA). Tap water and high-silica water were examples of drinking water containing minerals, while the calcium chloride solutions were used as a model of mineral-dissolved water with known concentrations. The concentration of Na, Ca, Mg, and Si in each type of water was measured using inductively coupled plasma mass spectrometry (ICP-MS) by Murata Keisokuki Service Co., Ltd. (Kanagawa, Japan). The humidifier was operated at approximately 80% power.

Characterization of particles from the humidifier

The mass concentration of particles in the chamber was measured by a Piezobalance dust monitor Model 3521 (Kanomax Japan Inc., Osaka, Japan). The number concentration of particles was measured by a portable particle counter CPC 3007 (Tokyo Dylec Co., Tokyo, Japan), which can count particles with 10–1000 nm diameter. The size distribution of particles (10–410 nm) was measured by a switch-mode power supplies system Model 3936 (TSI Inc., Shoreview, MN, USA) composed of a classifier DMA3081 (TSI Inc.) and a condensation particle counter CPC 3785 (TSI Inc.) at a flow rate of 0.6 L/min.

Airborne particles in the chamber were classified using a cascade impactor (NL-3-2.5c0.5c, Tokyo Dylec). Fractions of 0.5 – 2.5 μm and <0.5 μm were collected for 30 sec and 15 min, respectively, at a flow rate of 0.3 L/min. The fractionated particles were collected on a silicon wafer (SI-500452, Nilaco Co., Tokyo, Japan) or a collodion film-patched mesh (200 mesh Cu; Nisshin EM Co., Tokyo, Japan) by electrostatic force using a sampler for suspended particle matter, SSPM-100 (Shimadzu Co., Kyoto, Japan). To determine the form and elemental component of the particles, they were observed by a field emission-type scanning electron microscope/energy-dispersive X-ray spectrometer (FE-SEM/EDS) (JSM-6500 F, JEOL Ltd., Akishima, Tokyo, Japan) with accelerating voltage of 15.0 kV and a transmission electron microscope (TEM: JEM-1200EX II, JEOL) with accelerating voltage of 90.0 kV.

Exposure of mice to particles released from an ultrasonic humidifier

All animals were treated and handled in accordance with the national guidelines for care and use of laboratory animals and with the approval of the Tokyo University of Science Institutional Animal Care and Use Committee. Male ICR mice (10 weeks old) were purchased from Japan SLC Inc. (Hamamatsu, Shizuoka, Japan) and housed in a controlled room with *ad libitum* access to chow and water. After acclimation for 7 days, they were exposed by inhalation to an aerosol-containing vapor generated by an ultrasonic humidifier. The relative humidity was approximately 75% in the chamber with operating the humidifier. Tap water obtained in Noda-city, high-silica water, or ultrapure water were used to operate the ultrasonic humidifier for 7 days (8 hr/day [10:00 am – 6:00 pm] or whole day) or 14 days (whole day) (Table 1). After each exposure period, lung tissues and bronchoalveolar lavage fluid (BALF) were collected from each mouse under anesthesia by intraperitoneal injection of pentobarbital sodium.

BALF cell analysis

The cells in BALF were collected by centrifugation at 1,000 × *g* for 10 min and resuspended in phosphate-

Table 1 Experimental conditions for analysis of the effect of particles generated by ultrasonic humidifier on mouse lung

	Exposure time	Tested water
Experiment 1	8 hr/day, 7 days	Tap water/Ultrapure water
Experiment 2	8 hr/day, 7 days	High-silica water/Ultrapure water
Experiment 3	24 hr/day, 7 days	Tap water/Ultrapure water
Experiment 4	24 hr/day, 7 days	High-silica water/Ultrapure water
Experiment 5	24 hr/day, 14 days	High-silica water/Ultrapure water

buffered saline (pH 7.4). After counting the total number of cells, they were observed in a Giemsa-stained smear on a glass slide under a light microscope (BX51; Olympus Co., Tokyo, Japan). Statistical analysis was performed using an unpaired *t*-test and the level of significance was set at $P < 0.05$.

Total RNA isolation

Lung tissue was homogenized in Isogen (Nippon Gene Co., Ltd., Tokyo, Japan). Total RNA was isolated by chloroform, purified by isopropanol, precipitated in 70% ethanol according to the manufacturer's protocol and then suspended in RNase-free water. The RNA quantity was determined by absorption spectrophotometry at OD260 in a BioPhotometer plus (Eppendorf, Hamburg, Germany). Isolated RNA from each sample was provided for quantitative RT-PCR and microarray analyses.

Complementary DNA microarray

Total RNAs ($n = 4 - 5$/group) were pooled (45 μg) for each group and purified by RNeasy Micro Kit (Qiagen, Hilden, Germany). The integrity of RNA was evaluated by Bioanalyzer 2100 (Agilent Technologies Inc., Santa Clara, CA, USA). Complementary-DNA (cDNA) of each of the RNA samples was labeled by Cy3 and hybridized to the SurePrint G3 Mouse Gene Expression 8 × 60 K Microarray (Agilent Technologies) consisting of 62976 spots (containing probes for 24163 mRNAs) according to the protocol of Oncomics Co. Ltd. (Nagoya, Aichi, Japan). The microarray was then washed using Gene Expression Wash Pack (Agilent Technologies) and scanned by a DNA Microarray Scanner (Agilent Technologies). Scanner output images were normalized and digitalized by Feature Extraction software (Agilent Technologies) according to the Minimum Information About a Microarray Experiment (MIAME) guidelines [16].

Hierarchical cluster analysis

To extract gene sets for which differential expression was induced by airborne particles generated by the ultrasonic humidifier, microarray data from experiments 1–5 (Table 1) were hierarchically clustered using a complete linkage algorithm and Euclidean distance as the distance metric [17]. The analysis was performed using Cluster 3.0 [18] and the result was visualized by Java TreeView [19].

Functional analysis of microarray data

To better understand the biological meaning of the microarray results, functional analysis was performed using gene annotation by gene ontology (GO) and pathway. Genes were annotated with GO and pathway using an annotation file (gene2go.gz) provided by the National Center for Biotechnology Information (NCBI; Bethesda, MD, USA) [20] and c2.cp.v3.1.symbols.gmt by the Broad Institute (Cambridge, MA, USA) [21]. The annotations were updated on March 6, 2013. Enrichment factors for each GO and pathway were defined as $(nf/n)/(Nf/N)$, where nf is the number of flagged (differentially expressed) genes within the category, Nf is the total number of genes within that same category, n is the number of flagged genes on the entire microarray, and N is the total number of genes on the microarray. Statistical analysis was done with Fisher's exact test based on a hypergeometric distribution and then the GO and pathways with enrichment factors ≥3, $nf \geq 3$ and $P < 0.01$ were extracted.

Quantitative RT-PCR

Total RNA (1 μg) for each sample was treated by Dnase (Promega Co., Fitchburg, WI, USA) and then by M-MLV reverse transcriptase (Invitrogen Co., Carlsbad, CA, USA) to obtain first strand cDNA according to the manufacturer's instructions. Quantitative PCR was performed in a 96-well plate and an Mx3000P (Agilent Technologies) with SYBR Green Realtime PCR Master Mix (Thunderbird; Toyobo Co., Ltd., Osaka, Japan) and specific primers (Fasmac Co. Ltd., Atsugi, Kanagawa, Japan) or with Probe qPCR Master Mix (Thunderbird; Toyobo Co.) and primer (Fasmac)/probe (Biosearch Technologies Japan, Inc., Tokyo, Japan) sets for indicated genes (Additional file 1: Table S1). Statistical analysis was performed using an unpaired *t*-test and the level of significance was set at $P < 0.05$.

Immunohistochemistry

Lung tissue was fixed in phosphate-buffered (pH7.4) 4% formaldehyde, and then cryoprotected in phosphate-buffered 30% sucrose solution for 24–48 hr. Next, brains were frozen and cut into 4-μm sections using a cryostat (Tissue-Tek Cryo; Sakura Finetek Japan). Immunohistochemical visualization of a macrophage marker, F4/80, was performed using antibodies and avidin – biotin-peroxidase methods. After blocking endogenous peroxidase and preincubation with 10% normal horse serum, sections were treated overnight with primary rat monoclonal anti-F4/80 antibody (ab6640; Abcam plc, Cambridge, UK), secondary biotinylated donkey anti-rat IgG (AP189B; Merck Millipore) for 2 hr, and finally treated with an avidin – biotin-peroxidase complex (Vectastain ABC peroxidase kit, Vector Laboratories, CA, USA) for 4 hr. Sections were then reacted for peroxidase activity in a solution of 0.04% 3,3′-diaminobenzidene (DAB) in 0.1 M Tris–HCl buffer (pH 7.6) and 0.01% hydrogen peroxide water. Immunoreactive cells on sections were observed under BX51 light microscope. Quantitative analysis was performed on all sections. Statistical analysis was performed using an unpaired *t*-test and the level of significance was set at $P < 0.05$.

Electron microscopic analysis

Lung tissues and BALF cells were prefixed in cacodylate-buffered 2.5% glutaraldehyde (pH 7.4) for 24 hr, washed in cacodylate buffer, and postfixed with 2% osmium tetroxide (Nisshin EM) for 1 hr. After washing in cacodylate buffer, the tissue samples were dehydrated using a graded series of ethanol (up to 100%) and propylene oxide (Nisshin EM), and then embedded in Quetol 812 (Nisshin EM). Ultra-thin sections (80-nm thick) were cut on the ultra-microtome EMUC6 (Leica Microsystems K.K., Tokyo, Japan). Some sections were double-stained with uranyl acetate and lead citrate. They were then observed under the TEM (JEM-1200EX II) with accelerating voltage of 80–90 kV.

Results

Mineral and silica concentration of each water type

Tap water, high-silica water, RO water, and ultrapure water were subjected to ICP-MS analysis to measure the concentrations of Na, Ca, Mg, and Si (SiO_2: hydrated silica) (Table 2). Tap water contained 15–25 mg/L Na, 15–30 Ca, 4–7 Mg and 20–50 SiO_2. High-silica water contained 73 mg/L SiO_2. Most of the minerals and silica were absent in RO water, which contained only (3 mg/L) Na. No minerals and silica were detected in ultrapure water.

Concentration and size distribution of particles released from humidifier

First, we determined the mass and number concentrations and the peak size distribution of particles generated by an ultrasonic humidifier that was operated with each type of water in our chamber (Table 3). The results with tap water (Noda-city, and other area for which data not shown) were: mass concentration 0.35 – 0.50 mg/m^3, number concentration 3.5 – 7.5 × 10^4 particles/cm^3, and 155–195 nm peak size distribution (number distribution). The results obtained with high-silica water were similar to tap water. The mass concentration of particles generated by the humidifier with RO water was below the detection limit (<0.01 mg/m^3) but the number concentration was similar to tap water. The size distribution pattern with tap water and high-silica water was similar to a previous report [22] (Figure 1A). The humidifier generated visible fog (micro-sized water droplets) and submicro-sized residuals; however, because the SMA-CPC system could detect particles with diameter 10–410 nm, we characterized only the residuals as particles but not obtain size distribution data of the primary water droplets of the humidifier. The size of the particles generated by the humidifier using RO water was smaller to that of water types which contain a higher concentration of minerals and silica, e.g., tap water and high-silica water. The fog from the humidifier with ultrapure water did not contain non-volatile particles nor did it elicit any peak size distribution. The result with another type of pure water which originated from a PURELAB Option-7/15 Water Purification System (ELGA LabWater, Bucks, UK) was very similar to that with the ultrapure water (data not shown).

To investigate the correlations between mineral concentration in water and each parameter of generated particle, we characterized the particles released from the ultrasonic humidifier using water containing serial concentrations of calcium chloride solution (4–400 mg/L Ca) (Table 3). The concentration of calcium chloride in water was positively correlated with the mass and number concentrations (Figure 1C and D) and the peak size distribution (Figure 1B and E) of generated particles. The correlation of the concentration of dissolved material in water with the mass concentration of particles generated was linear (r =0.97) (Figure 1C), whereas the correlation with the number concentration was logarithmic (r =0.98) (Figure 1D). These correlations were also observed in particles from the humidifier with serial concentrations of sodium chloride solution (4–400 mg/L Na) (data not shown). The mass concentration of the aerosol particles was also correlated with total mineral concentration of tap water, high-silica water and RO water (Figure 1A).

Form and elemental composition of particles released from humidifier

FE-SEM images showed that the humidifier operated with tap water or high-silica water released a large number of spherical-formed amorphous <0.5 μm particles and 0.5 – 2.5 μm agglomerates (Figure 2A – C). The particles were deformed under extremely high humidification (Figure 2D, E). TEM images also showed that the form of particles from the humidifier operated with tap water (Figure 2F) or high-silica water (Figure 2G) were spherical. The electron density of the particles was inhomogeneous under TEM observation, indicating that the particles were

Table 2 Mass concentration of mineral and silica in each type of water

	Na (mg/L)	Ca (mg/L)	Mg (mg/L)	SiO_2 (mg/L)	Total (mg/L)
Tap water	18	25	5.6	24	73
High-silica water	15	12	3.7	73	104
RO water	3	<0.1	<0.1	<0.1	3
Ultrapure water	<0.1	<0.1	<0.1	<0.1	<0.1

Table 3 Concentration and size of airborne particles released from ultrasonic humidifier for each type of water

Used water	Mass concentration (mg/m^3)	Number concentration (#/cm^3)	Peak of size distribution (nm)
Tap water	0.46 ± 0.03	(5.0 ± 1.1) × 10^4	183 ± 9
High-silica water	0.58 ± 0.04	(3.6 ± 0.0) × 10^4	180 ± 3
$CaCl_2$ (400 mg/L Ca)	1.66 ± 0.16	(6.3 ± 0.5) × 10^4	>410
$CaCl_2$ (200 mg/L Ca)	1.26 ± 0.19	(4.2 ± 0.3) × 10^4	356 ± 11
$CaCl_2$ (80 mg/L Ca)	0.46 ± 0.11	(5.0 ± 0.1) × 10^4	283 ± 9
$CaCl_2$ (40 mg/L Ca)	0.12 ± 0.03	(4.5 ± 0.0) × 10^4	222 ± 4
$CaCl_2$ (10 mg/L Ca)	0.08 ± 0.01	(3.4 ± 0.1) × 10^4	123 ± 4
$CaCl_2$ (4 mg/L Ca)	0.02 ± 0.01	(2.7 ± 0.3) × 10^4	108 ± 2
RO water	<0.01	(4.4 ± 0.6) × 10^4	90 ± 2
Ultrapure water	<0.01	(0.7 ± 0.0) × 10^4	Not determined

Data are shown as mean ± SD, calculated from 5 repeats of 2 min analyses.

composed of multiple elements. EDS analysis showed the particles derived from tap water were composed of Na, Mg, Si, S (sulfate), and Ca, which were contained in tap water (Figure 2H).

Effect of particles released from ultrasonic humidifier on mRNA expression in the lung

Next, we conducted microarray analysis to investigate the effect of particles from the humidifier on the lung. The effect of the particles was determined by mRNA expression of tested water groups compared to that of ultrapure water groups in each experiment (Table 1). A total of 15984 mRNAs were detected with quantitative fluorescence signals from the lung tissue samples. Hierarchical clustering revealed that 429 mRNAs were differentially expressed (238 upregulated and 191 downregulated) by particles derived from tested water (tap water or high-silica water) (Additional file 1: Figure S1). Expression change of some genes was correlated with the dose in the experiment 2, 4 and 5 using high-silica water. These 429 genes were enriched in 17 GO (Table 4) and 12 pathways (Table 5). The largest GO and pathway were

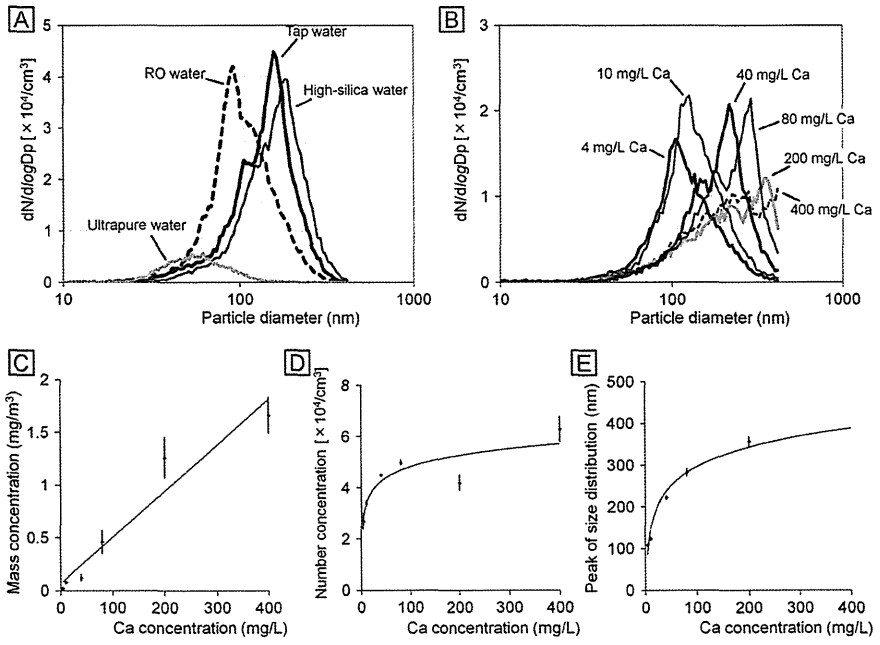

Figure 1 Size distribution of airborne particle released from ultrasonic humidifier with each water type. Number distribution of the size of particles from humidifier with **(A)** tap water, high-silica water, ultrapure, and **(B)** serial concentrations of calcium chloride solution are shown. The correlation of calcium chloride concentration with **(C)** mass concentration, **(D)** number concentration, and **(E)** peak size distribution are also shown.

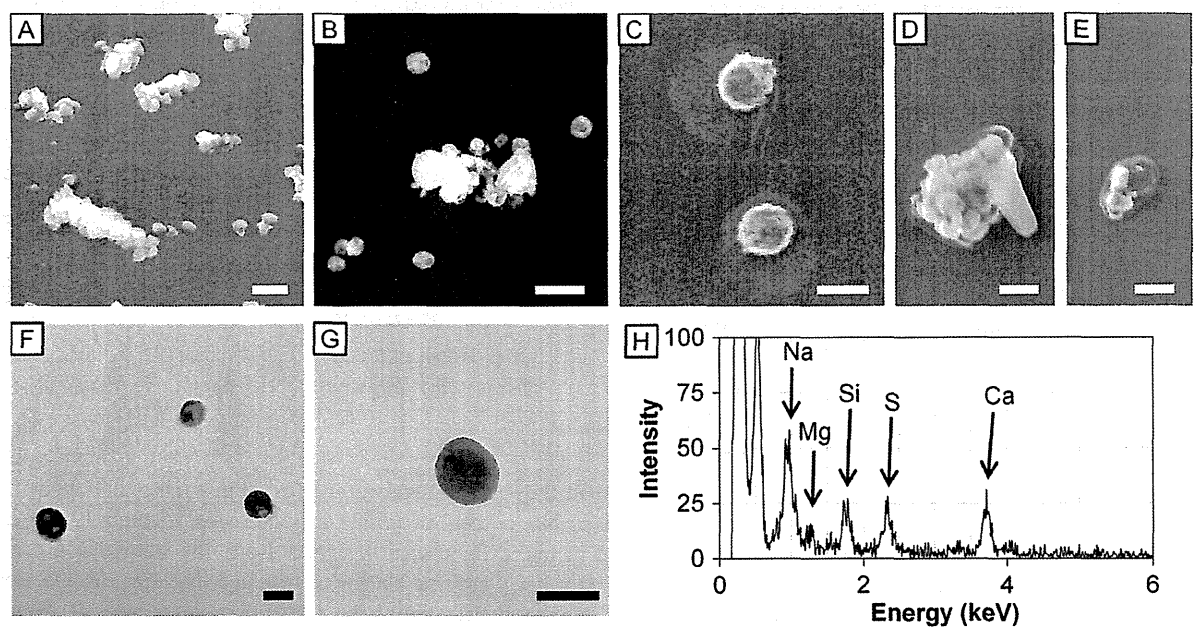

Figure 2 FE-SEM images, TEM images and EDS spectrum of particles released from ultrasonic humidifier. FE-SEM images of particles (0.5 – 2.5 μm) released from the humidifier with **(A)** tap water and **(B)** high-silica water under humidity 75%; particles (<0.5 μm) from the humidifier with tap water under **(C)** humidity 75% and **(D, E)** 99% are shown. TEM image of particles (<0.5 μm) from the humidifier with **(F)** tap water and **(G)** high-silica water under humidity 75%. Scale bars represent **(A, B)** 1 μm, **(C, F, G)** 200 nm, and **(D, E)** 500 nm. **(H)** EDS spectrum of the particle **(C)** is shown. The peaks of Na, Mg, Si, S, and Ca were detected at 0.97, 1.26, 1.78, 2.33, and 3.71 keV, respectively.

Table 4 Significantly enriched GO categories from the microarray data

Gene ontology	Enrichment factor	P-value
Mitosis	3.05	<0.001
Meiosis	5.35	0.001
Regulation of axonogenesis	8.61	0.001
Antigen processing and presentation of peptide or polysaccharide antigen via MHC class II	13.7	0.001
Chromosome, centromeric region	3.50	0.001
Kinetochore	3.80	0.001
Decidualization	12.2	0.002
MHC class II protein complex	12.2	0.002
Peptide antigen binding	12.2	0.002
Platelet activation	7.32	0.002
Gamma-aminobutyric acid signaling pathway	11.0	0.002
Motile cilium	6.65	0.003
Retinol metabolic process	9.98	0.003
Adenylate cyclase-activating G-protein coupled receptor signaling pathway	6.36	0.003
Antigen processing and presentation of exogenous peptide antigen via MHC class II	8.44	0.005
Chromosome segregation	3.60	0.006
Axon part	7.32	0.007

mitosis (17 genes) and cell adhesion molecules (8 genes) (Additional file 1 Table S2). Among the 8 genes in cell adhesion molecules, upregulated *H2-DMb1* and downregulated *H2-Ab1*, *H2-Eb1*, *H2-Q2* were associated with major histocompatibility complex (MHC) molecules, and endocytosis followed by antigen processing. Quantitative RT-PCR data showed that expression levels of a monocyte chemoattractant chemokine *Ccl2* and a chemokine related to inhalation of silica particles *Cxcl1* [23] were not affected by the particles released from the ultrasonic humidifier operated with tap water or high-silica water (Figure 3). Expression of an inflammatory cytokine *Tnf* was at quite low level in the lung of any groups.

Effect of particles released from ultrasonic humidifier on histology of the lung and alveolar macrophage

HE-stained images did not show any remarkable changes or cell proliferation in lung after inhalation of particles from the humidifier with tap water or high-silica water (24 hr/day, 7–14 days). The lung tissues obtained from experiment 5 (24 hr/day for 14 days inhalation with the commercial high-silica water *vs.* ultrapure water; Table 1) were also subjected to analysis by immunohistochemistry and TEM. TEM observation of the lung tissues (Figure 4A) and BALF cells (Figure 4B) revealed that alveolar macrophages endocytosed the particles. The endocytosed particles showed a high contrast without staining by uranyl